SAND REPORT
SAND2002-3419
Unlimited Release
Printed October 2002

A Dilute Spray Model for Fire Simulations: Formulation, Usage and Benchmark Problems

Paul E. DesJardin and Louis A. Gritzo

Prepared by
Sandia National Laboratories
Albuquerque, New Mexico 87185 and Livermore, California 94550

Sandia is a multiprogram laboratory operated by Sandia Corporation,
a Lockheed Martin Company, for the United States Department of Energy's
National Nuclear Security Administration under Contract DE-AC04-94-AL85000.

Sandia National Laboratories

Issued by Sandia National Laboratories, operated for the United States Department of Energy by Sandia Corporation.

Available to DOE and DOE contractors from
U.S. Department of Energy
Office of Scientific and Technical Information
P.O. Box 62
Oak Ridge, TN 37831

Telephone: (865)576-8401
Facsimile: (865)576-5728
E-Mail: reports@adonis.osti.gov
Online ordering: http://www.doe.gov/bridge

Available to the public from
U.S. Department of Commerce
National Technical Information Service
5285 Port Royal Rd
Springfield, VA 22161

Telephone: (800)553-6847
Facsimile: (703)605-6900
E-Mail: orders@ntis.fedworld.gov
Online order: http://www.ntis.gov/help/ordermethods.asp?loc=7-4-0#online

SAND 2002-3419
Unlimited Release
Printed August, 2002

A Dilute Spray Model for Fire Simulations: Formulation, Usage and Benchmark Problems

Paul E. DesJardin and Louis A. Gritzo
Fire Science and Technology, 9132
Sandia National Laboratories
Albuquerque, New Mexico 87185

Abstract

The focus of this work is to develop a two-phase spray model for application to unsteady fire simulation for the dispersion of dilute liquid fuel or fire suppressant sprays. The model is based on a stochastic separated flow (SSF) approach for which droplet transport equations are integrated in time to account for mass, momentum and energy transfer to the liquid phase. Turbulence models for parcel and sub-parcel droplet dispersion, spray breakup and spray collision are also developed and implemented. Two-way coupling between the liquid spray and the gas phase is accomplished through a numerical sub-cycling procedure. A strategy plan for spray model verification and validation is summarized and results presented for selected cases. The problems examined thus far indicate that the approach provides a robust and accurate means to solve dispersed phase spray transport problems for application to fire phenomena.

Acknowledgment

This work is supported by the Office of Live Fire Test and Evaluation under the Safety and Survivability of Aircraft Initiative. Sandia is a multiprogram laboratory operated by Sandia Corporation, a Lockheed Martin Company, for the United States Department of Energy under Contract DE-AC04-94AL85000.

NOMENCLATURE

Roman Symbols

A_d	= Droplet surface area $[m^2]$
A_{inj}	= Injector cross sectional area $[m^2]$
A_g	= Gas phase surface area in a phase averaging volume $[m^2]$
A_l	= Droplet surface area in a phase averaging volume $[m^2]$
B_m	= Mass transfer or Spaulding number
B_t	= Thermal transfer number
C_{Bi}	= Transition Biot number parameter
C_D	= Coefficient of drag
C_F, C_b, C_k, C_d	= Taylor Analogy Breakup (TAB) model constants
C_P	= Specific heat at constant pressure $[J/Kg-K]$
C_v	= Specific heat at constant volume $[J/Kg-K]$
D_d	= Droplet diameter $[m]$
D_m	= Molecular diffusivity $[m^2/s]$
F_{b_j}	= Droplet body force $[kg-m/s^2]$
F_{D_j}	= Droplet drag force $[kg-m/s^2]$
g_j	= Acceleration due to gravity $[kg-m/s^2]$
G or G^*	= Spatial filtering function $[1/m^3]$
h_{lg}	= Heat of vaporization $[J/Kg]$
h	= Heat transfer coefficient $[J/(m^2-s-K)]$
h	= Total enthalpy (*i.e.*, $h = h_{sensible} + h_{chemical}$) $[J/kg]$
h_m	= Mass transfer coefficient $[m/s]$
H	= Heaviside function
k	= Turbulent kinetic energy $[m^2/s^2]$
k	= Thermal conductivity $[kg/K-s-m^2]$
L_e	= Characteristic turbulent eddy length scale $[m]$
m	= Mass $[kg]$

NOMENCLATURE (continued)

$\dot{m}$	= Droplet mass loss rate $[kg/s]$
MFR	= Mass flow rate $[kg/s]$
n_d	= Number of drops per computational parcel
N	= Number of statistical realizations
N_p	= Total number of computational parcels
N_d	= Total number of drops
$N_{d_{CELL}}$	= Total number of drops in a cell volume
p	= Pressure $[kg/(m-s^2)]$
q	= Rosin-Rammler drop size distribution parameter
q_j	= Heat conduction $[J/(m^2-s)]$
q_{m_j}	= Mass diffusion $[Kg/(m^2-s)]$
r_d	= Droplet radius $[m]$
RN	= Random number
S_d^*	= Spray source terms due to non-evaporative processes
S_d^{**}	= Spray source terms due to evaporative processes
S_d	= Total spray source terms, $S_d = S_d^* + S_d^{**}$
T	= Temperature $[K]$
u_j, u, v, w	= Velocity $[m/s]$
$\dot{Q}_c$	= Droplet heating or cooling rate due to convection $[J/s]$
$\dot{Q}_e$	= Droplet cooling due to evaporation $[J/s]$
$\dot{Q}_{comb}$	= Heat release due to combustion $[J/s]$
$\dot{Q}_{rad}$	= Heat gain or loss due to radiation $[J/s]$
X	= Rosin-Rammler drop size distribution parameter
Y_i	= Mass fraction of the i^{th} species
y	= Non-dimensional droplet displacement in the TAB model
V_C	= Volume of the computational cell volume $[m^3]$
V_T	= Phase averaging volume $[m^3]$

NOMENCLATURE (continued)

Greek Symbols

α	= Film temperature weighting parameter
α_s	= Start angle for spray injector [radians]
α_e	= End angle for spray injector [radians]
δ_{ij}	= Kronecker delta function
Δ_f	= Phase averaging filter width $[m]$
Δ_{f_T}	= Phase averaging filter width in transformed computational space
Δx_j	= Grid cell dimension in the j^{th} direction $[m]$
Δt	= Numerical time step $[s]$
ε	= Rate in change of turbulent kinetic energy $[m^2/s^3]$
ρ	= Density $[kg/m^3]$
ϕ	= Void fraction, V_g/V_T
ϕ, ψ, θ	= Angles *[radians]*
σ	= Square root of standard deviation or root mean square
τ_C	= Droplet cross trajectory time $[s]$
τ_d	= Droplet relaxation time $[s]$
τ_e	= Turbulent eddy turnover time $[s]$
τ_{ij}	= Viscous stress tensor (*i.e.*, $\tau_{ij} = -\frac{2}{3}\mu(\partial u_k/\partial x_k) + \mu(\partial u_j/\partial x_i + \partial u_j/\partial x_i)$) $[kg/(m-s)]$
μ	= Molecular viscosity $[kg/m-s]$
ν	= Kinematic viscosity $[m^2/s]$
ω	= Droplet frequency used in TAB model $[Hz]$

Nondimensional Parameters

Bi	= Thermal Biot number
Le	= Lewis number
Pr	= Prandtl number
Re	= Reynolds number
Sc	= Schmidt number
St	= Stokes number
We	= Weber number

NOMENCLATURE (continued)

Subscript Symbols

c	= Concentration
d	= Liquid property
f	= Droplet film property
g	= Gas property
T	= Transformed computational space
inj	= Injector property
$\perp$	= Direction perpendicular to droplet trajectory or spray injector
$\parallel$	= Direction parallel to droplet trajectory or spray injector
1	= Property before drop collision
2	= Property after drop collision

Abbreviations

ARL	= Army Research Laboratory
CDF	= Cumulative Probability Distribution Function
CE	= Commutation error
DSF	= Deterministic Separated Flow
JPDF	= Joint Probability Density Function
LES	= Large Eddy Simulation
LHF	= Locally Homogeneous Flow
NRL	= Naval Research Laboratory
PDF	= Probability Density Function
PDPA	= Phase Doppler Particle Anemometry
RANS	= Reynolds Averaged Navier Stokes equations
RMS	= Root Mean Square
SIMPLE	= Semi-Implicit Pressure Linked Equations
SGS	= Subgrid Scale
SSF	= Stochastic Separated Flow
SET	= Surface Exchange Term
SEET	= Surface Exchange Error Term
TAB	= Taylor Analogy Breakup Model
V&V	= Verification and Validation

NOMENCLATURE (continued)

Mathematical Operators

β'	= Turbulent time fluctuation of the β quantity from $\bar{\beta}$
$\bar{\beta}$	= Time average of the quantity β
$\langle\beta\rangle$	= Phase average of the quantity β
$\hat{\beta}$ or $\widehat{\beta}$	= Intrinsic phase average of the quantity β, note, $\hat{\beta} = \langle\beta\rangle/\phi$
$\tilde{\beta}$	= Density weighted intrinsic phase average, *i.e.*, $\tilde{\beta} \equiv \widehat{\rho\beta}/\hat{\beta}$

Constants

π	= Pi [3.14159.....]

TABLE OF CONTENTS

LIST OF TABLES

LIST OF FIGURES

Figure Page

CHAPTER 1 INTRODUCTION AND MOTIVATION

The use of computational fluid dynamics (CFD) is quickly becoming a useful tool for prediction of fire phenomena. One example is the VULCAN fire physics code jointly developed by Sandia National Laboratories and the foundation for scientific and industrial research at the Norwegian Institute of Technology (SINTEF). The code is based on a Reynolds averaged Navier Stokes (RANS) formulation employing a standard $k-\varepsilon$ for turbulence model [1], the eddy dissipation concept (EDC) combustion model[2], soot model [3], and a radiation [4] model for participating media. Previous studies using VULCAN have ranged from large outdoor open fires [6] to smaller enclosed dry bay fires [7]. The focus of this work is to incorporate a spray modeling capability into VULCAN to account for the dispersal of fuel spray or liquid fire suppressants. In addition, the same modeling explored in this study could also be adapted to other codes using similar, or alternative formulations, such as the use of Large Eddy Simulation [98].

The targeted application for the spray model development is to address the thermal threat from a fire induced by a live fire event in dry bay and cargo crew compartments of DoD military vehicles. The long term objective is to predict the lethality and the likelihood of component failure due to fire thermal loading. It is expected this information will provide guidance to future experimental live-fire tests and detailed data for probabilistic vulnerability assessments studies. A live-fire event test consists of the penetration of a military vehicle by an incendiary ammunition round, resulting in a punctured fuel tank or possibly a pressurized hydraulic line. The flash from the incendiary combined with the highly atomized fuel spray can result in an ignition event that may lead to a sustained pool fire as illustrated in Fig. 1-1.

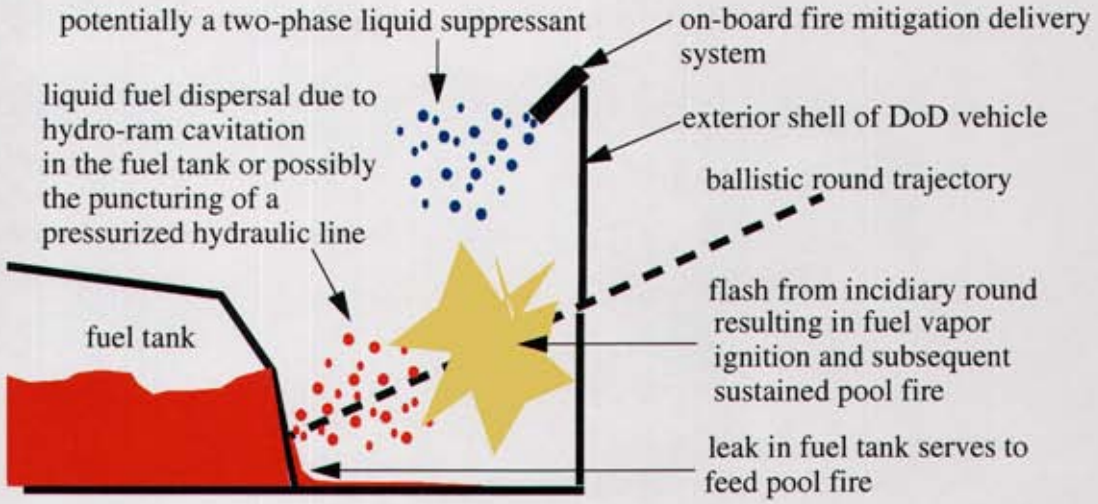

Figure 1-1 Live-fire event illustrating liquid fuel spray ignition and sustained pool fire.

Once a fire is detected in the dry bay, or cargo compartment, then a fire mitigation delivery system is activated. Some of the newer agents considered for fire suppression have higher boiling temperatures and may be released in a liquid state. The transport of liquid fire suppressant agent, as opposed to a total flooding gaseous agent, is highly sensitive to the local

thermo-physical flow environment and requires careful attention to the modeling of droplet processes for numerical simulation of this event.

Droplet transport and exchange of mass, momentum and energy with the surrounding gas from evaporation occurs at time and length scales on the order of mircoseconds and micrometers, respectively. Resolving these processes from first principals is currently not computationally feasible for any engineering problem of interest in the forseeable future. Subgrid scale models (SGS) are therefore required to account for droplet transport and evaporative processes. Modeling spray transport requires several subcomponent modeling assumptions to account for the exchange of mass, momentum and energy between the liquid and gas phases. In order to gain confidence that these approximations are valid for the live-fire problem, verification and validation (V&V) testing is needed. Verification is the process of ensuring the CFD program is free from any errors due to coding (*i.e.*, bugs). Validation is the process of assessing the uncertainty in the predictive capability of the models. Formal V&V of a new models is a necessary, but often time intensive process [8]. The scope of the current study is not to present a formal V&V of the spray submodels, but rather demonstrate the capability of the approach and suggest problem sets that may be used in future studies for a more rigorous V&V effort.

The next chapter defines the mathematical treatment of two-phase sprays in VULCAN and the modeling assumptions in detail. Chapter 3 discusses the numerical implementation of the spray model into VULCAN and user input parameters for controlling numerical stability of the solution. Chapter 4 defines a preliminary plan for the spray model verification and validation and results presented for a selected number of problems. The information in this strategy could serve as a basis for a more comprehensive V&V effort in the future. Lastly, summary and conclusions are drawn in chapter 5 and areas for future improvements are outlined.

CHAPTER 2 MATHMATICAL FORMULATION AND MODEL DEVELOPMENT

Several approaches can be used to formulate a two-phase system using either space averaging [91-98] or probabilistic descriptions [35,99,100]. The approach taken here is based on a spatial or phase-averaging. The specifics of phase-averaging are summarized in appendix A. In this approach, the governing equations of mass, momentum and energy are averaged in space introducing additional terms requiring explicit SGS modeling, and source terms that account for mass, momentum and energy transfer from the droplets to the gas phase. These source terms are determined from the liquid phase transport equations that track the evolution of droplets as they are transported in the carrier gas. The following subsections detail the modeling of the droplet transport as well as to construction of the spray source terms needed for the phase averaged transport equations.

2.1 Spray Transport Equations

A stochastic separated flow (SSF) model [9] is used to represent the liquid phase of the flow. The SSF model is implemented using Lagrangian particles which can either represent individual droplets or groups of droplets referred to as parcels or elements [10]. The dynamics of these droplets are governed by a set of ordinary differential equations (ODE's) accounting for conservation mass, momentum and energy. Derivations of these ODE's can be found in several excellent texts on droplet transport [10,19] and so are not repeated in this report.

A "thin film" assumption [13] is used to approximate the two-phase liquid-gas interface at the surface of each droplet. The following subsections summarize the transport equations for evaporating droplets. In these equations, the subscripts "d", "g", and "f " denote properties of the droplet, gas and film, respectively, as shown below in Fig. 2-1.

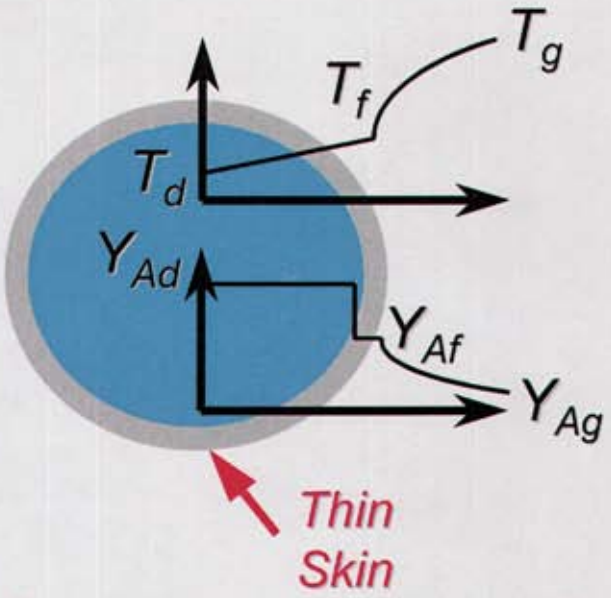

Figure 2-1 Property variation in droplet using a thin skin model.

2.1.1 Conservation of Mass and Species

The loss of mass from evaporation of the liquid droplet is described using the following transport equation:

$$\frac{dm_d}{dt} = \dot{m}_d = -\pi D_d \frac{\mu_f}{Sc_f} B_m Sh_f \tag{2-1}$$

where m_d is the mass of the droplet and ρ_f and ν_f are the density and kinematic viscosity at the film thermodynamic state. The film being defined as the liquid-gas interface on the droplet surface is shown in Fig. 2-1. The parameter, $B_m (= (Y_f - Y_g)/(Y_d - Y_f))$, is the Spaulding or mass transfer number and characterizes the concentration gradients at the film interface. The Sherwood number, Sh_f $(= h_m D_d / D_{m_f})$, accounts for evaporation due to convection and is expressed in terms of the particle Reynolds number, Re_d $(= \rho_g D_d |u_{g_j} - u_{d_j}| / \mu_g)$, and film Schmidt number, Sc_f $(= \nu_f / D_{m_f})$ using the Ranz-Marshall correction [24]: $Sh_f = 2[1 + Re_d^{1/2} Sc_f^{1/3}/3]\log(1 + B_m)/B_m$. The properties at the film conditions still need to be specified and will be discussed on the evaluation of the film thermophysical state in section 2.2.

2.1.2 Conservation of Momentum

The momentum equations for a small rigid sphere in non-uniform flow are derived by Maxey and Riley [14]. The momentum source terms for these equations include aerodynamic drag, static pressure gradient, virtual-mass, Basset, Saffman lift and body forces [11]. As discussed by Faeth [13], if the ratio of particle to gas densities is large (*i.e.*, $\rho_d / \rho_g \gg 1$), then the predominate forces consist of only the drag, F_{D_j}, and body forces, F_{b_j}, leading to considerable simplification of the momentum equations to the form:

$$m_d \frac{du_{d_j}}{dt} = F_{D_j} + F_{b_j} = \frac{\pi}{8} \rho_g D_d^2 C_D |u_{g_j} - u_{d_j}| (u_{g_j} - u_{d_j}) + g_j m_d \tag{2-2}$$

where u_{d_j} and u_{g_j} are the droplet and gas phase velocities, D_d, is the droplet diameter, and ρ_g is the gas phase density. The last term on the right hand side is the body force term due gravity. As a starting point, the coefficient of drag, C_D, is modeled using the standard drag coefficient relations for a sphere in uniform flow [13, 14],

$$C_D = \begin{cases} 24(1 + Re_d^{2/3}/6)/Re_d & for\ Re_D < 1000 \\ 0.424 & for\ Re_D \geq 1000 \end{cases} . \tag{2-3}$$

More sophisticated treatments could be pursued to account for non-spherical particles [15] and dense spray regimes [35].

2.1.3 Conservation of Energy

The droplet energy expressed in terms of droplet temperature, T_d, accounts for the heat transfer due to convection ($\dot{Q}_{d_c}$) and evaporation ($\dot{Q}_{d_e}$) processes and has the form:

$$m_d C_{v_d} \frac{dT_d}{dt} = \dot{Q}_c + \dot{Q}_e = \pi D_d \frac{\mu_f C_{P_f}}{Pr_f}(T_g - T_d) Nu_f + \dot{m}_d h_{lg} \tag{2-4}$$

where C_{v_d} is the liquid droplet specific heat, h_{lg}, is the heat of vaporization and Pr_f $(= C_{P_f}\mu_f / k_f)$ is the film Prandtl number. The thermal transfer number, $B_t = C_{P_f}(T_g - T_f)/h_{lg}$, characterizes the temperature gradient at the film surface and can be expressed in terms of the Spaulding number under steady-state heat and mass transfer conditions as: $B_t = (1 + B_m)^{Le_f} - 1$, where Le_f $(= Sc_f / Pr_f = k_f / (\rho_f C_{P_f} D_{m_f}))$ is the film Lewis number [16]. The film Nusselt number, Nu_f $(= h_d D_d / k_f)$, accounts for heat transfer due convection and is modeled similar to the Sherwood number as: $Nu_f = 2[1 + Re_d^{1/2} Sc_f^{1/3}/3]\log(1 + B_m)/B_m$.

2.2 Evaluation of Film Properties

In Eqs. (2-1)-(2-4), the film properties are required to complete the description of the source terms to account for mass, momentum and heat exchange with the gas phase. The thermodynamic properties at the film for liquid (species A) and surrounding gas (species B) interface are determined using one of two approaches. The first is based on a quasi-steady-state droplet heat and mass transfer process and the second assumes quasi-steady-state droplet mass transfer. Both models are considered "thin skin" approximations [9] where the temperature and species distributions in and around the droplet are broken into three regions, as shown in Fig. 2-1. These regions consist of the temperature and species conditions at the droplet center ($Y_{A_{d_c}}$, T_d), at the film interface or droplet surface (Y_{A_f}, Y_{B_f}, T_f), and in the surrounding gas (Y_{A_g}, Y_{B_g}, T_g), as illustrated in Fig. 2-1.

2.2.1 Thin Skin Model for Quasi-steady-state Heat and Mass Evaporation

The first model to determine the thermodynamic film state is based on assuming steady-state mass and heat transfer to the droplet. By neglecting the internal circulation of the droplet, assuming saturation conditions at the film surface, and only considering the mass and energy transfer at the droplet surface due to diffusion and evaporation, then coupling functions between mass and energy can be obtained allowing for a closed form solution of the species and temperature distribution as a function of droplet radius [16]. Using this solution, along with assuming a Clausius-Clapeyron relation to describe the change in saturation conditions, then an iterative procedure can be devised to determine the film surface thermophysical properties as follows:

1. Guess an initial value for Y_{A_f}.
2. Determine mass (Spaulding) and thermal transfer numbers:

   $B_m = (Y_{A_f} - Y_{A_g})/(Y_{A_d} - Y_{A_f})$ and $B_t = (1 + B_m)^{Le_f} - 1$.
3. Calculate film temperature assuming saturation conditions: $T_f = T_g - B_t h_{lg_A}/C_{P_{A_f}}$.
4. Calculate the heat of vaporization using the relation from Watson [17,18]:

   $h_{lg_A} = h_{lg_{A_{ref}}}[(T_{C_A} - T_f)/(T_{C_A} - T_{ref})]^{0.38}$ where T_{C_A} is the critical temperature for species A and $h_{lg_{A_{ref}}}$ is a user specified reference heat of vaporization for species A at a given reference temperature, T_{ref}, and partial pressure, $P_{A_{ref}}$.
5. Calculate saturation partial pressure using Clausius-Clapeyron relation:

   $\ln(P_{A_f}/P_{A_{ref}}) = -h_{lg_A}\left(\left(\frac{1}{T_f} - \frac{1}{T_{ref}}\right)/R_A\right)$ where R_A is the gas constant for species A.

   Note: If $P_{A_f} > P$, then P_{A_f} is set equal to P and iterate using Clausius-Clapeyron and Watson relations to find T_f, *i.e.*, the fluid is boiling at the droplet surface.
6. Recalculate species mass fraction using partial pressures: $Y_{A_f} = \frac{P_{A_f}}{P}\frac{MW_A}{MW_{mix_f}}$ where

   $MW_{mix_f} = (Y_{A_f}/MW_A + (1 - Y_{A_f})/MW_B)^{-1}$.
7. Compare calculated Y_{A_f} from step 6 with guessed value from step 1. and repeat steps 1-6 using a Newton-Raphson-Secant iteration until convergence is achieved.
8. Once convergence is achieved then calculate mixture film surface density:

   $\rho_{mix_f} = \left(\frac{P_{A_f}}{R_A} + \frac{P - P_{A_f}}{R_B}\right)/T_f$.

2.2.2 Thin Skin Model for Quasi-steady-state Mass Evaporation

The quasi-steady-state heat and mass evaporation model works well for gradual changes in droplet temperature (*i.e.*, $dT/dt \approx 0$). However, the quasi-steady-state heat transfer assumption breaks down when the drops are suddenly exposed to either extremely high gas temperatures (*e.g.*, a spray flame) or when there is significant heat and mass loss due to evaporation (*e.g.*, suppression). For these cases, non-physical temperatures may result at the film surface using the procedure outlined in section 2.2.1, or the iteration solution procedure may not converge at all. More sophisticated treatments of the internal flow dynamics of the droplet are available, such as the Hill's vortex model [12,19], and may help alleviate these problems. These approaches require numerical spatial descritization of each drop, requiring substantially more computational expense. Rather than increasing computational cost, an alternative simpler procedure is devised to prescribe the temperature at the droplet surface using a linear weighting of the droplet temperature and the surrounding gas temperature, expressed as:

$T_f = (1-\alpha)T_d + \alpha T_g$. The weighting function, α, may be either set to a fixed value such as $\alpha = 1/3$ leading to the so called "1/3 rule" [10] or is set based on a local thermal Biot number, Bi $(= hD_d/k_d)$, as: $\alpha = MIN(C_{Bi}Bi, 1)$. The constant C_{Bi} defines the transition Bi number for which the droplet film temperature is equal to the surrounding gas temperature, *i.e.*, $T_f = T_g$, as shown below in Fig. 2-2.

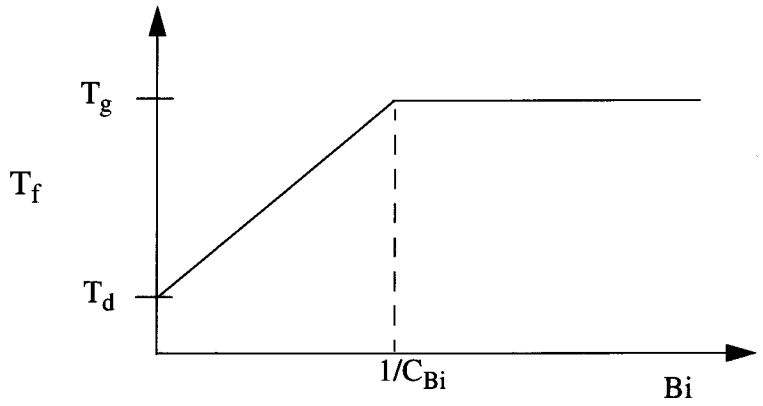

Figure 2-2 Film temperature as a function of droplet thermal Biot number.

In general, the choice of α is application specific and should be calibrated using either experimental data or detailed simulations of single droplet evaporation. Through numerical trial and error, a value of $C_{Bi} = 0.5$ has shown to provide reasonable results over a wide range of evaporation time scales.

Physically, these approximations assume that mass diffusion is fast enough that evaporation processes are in steady state while the thermal diffusion processes are not, which is consistent with the fact that $Le_f < 1$ for many of the spray applications of interest [19]. This second scheme has proven to be robust for determining the film conditions and is used for all the examples in this study that require heat and mass transfer from the drops due to evaporation. The overall procedure to determine film thermophysical state properties is summarized as follows:

1. Calculate film temperature using a weighted average: $T_f = (1-\alpha)T_d + \alpha T_g$, where α is either set to a fixed value or determined from $\alpha = MIN(C_{Bi}Bi, 1)$.
2. Calculate the heat of vaporization using the relation from Watson [17,18]: $h_{lg_A} = h_{lg_{A_{ref}}}[(T_{C_A} - T_f)/(T_{C_A} - T_{ref})]^{0.38}$ where T_{C_A} is the critical temperature for species A and $h_{lg_{A_{ref}}}$ is a user specified reference heat of vaporization for species A at a given reference temperature, T_{ref}, and partial pressure, $P_{A_{ref}}$.
3. Calculate saturation partial pressure using Clausius-Clapeyron relation:

$\ln(P_{A_f}/P_{A_{ref}}) = -h_{lg_A}\left(\left(\frac{1}{T_f}-\frac{1}{T_{ref}}\right)/R_A\right)$ where R_A is the gas constant for species A.

Note: If $P_{A_f} > P$, then set P_{A_f} is set equal to P and iterate using Clausius-Clapeyron and Watson relations to find T_f, *i.e.*, the fluid is boiling at the droplet surface.

4. Calculate thermal transfer number: $B_t = C_{P_f}(T_g - T_f)/h_{lg}$
5. Calculate mass fraction of species A at surface: $Y_{A_f} = \left(\frac{MW_A}{MW_B}\right)/\left[\frac{P}{P_{A_f}} + \frac{MW_A}{MW_B} - 1\right]$
6. Calculate mass transfer number or Spaulding number: $B_m = (Y_{A_f} - Y_{A_g})/(Y_{A_d} - Y_{A_f})$.

   Note: If $P_{A_f} > P$, then set $P_{A_f} = P$ (*i.e.*, droplet surface is boiling, so $dT/dt \approx 0$) and $B_m \to \infty$ so instead B_m is set equal to $(1 + B_t)^{1/Le_f} - 1$ which is the same as the steady-state heat and mass transfer approximation of 2.2.1.
7. Calculate molecular weight and density at the film surface:

   $MW_{mix_f} = (Y_{A_f}/MW_A + (1 - Y_{A_f})/MW_B)^{-1}$ and $\rho_f = \left(\frac{P_{A_f}}{R_A} + \frac{P - P_{A_f}}{R_B}\right)/T_f$.

2.3 Turbulence Models

The relations given in Eqs. (2-1)-(2-4) are expressed in terms of the local instantaneous thermodynamic states around each droplet. In a RANS formulation, these quantitates are unknown since only time averaged values are available. Turbulence models are introduced at the parcel and sub-parcel level to account for local fluctuations in the velocity field while the rest of the thermophysical variables are set equal to their corresponding time averaged values for lack of established models. These models serve to increase the droplet dispersion, mimicking the effects of unresolved turbulent eddies. These unresolved turbulent motions are especially significant for release of a high pressure spray that generates high levels of turbulent kinetic energy. These unresolved turbulent motions are decomposed into parcel and sub-parcel models.

2.3.1 parcel turbulence model

The parcel turbulence model accounts for the effects of turbulent eddies perturbing the parcel trajectory and is based on the random walk model of Gosman and Ioannides [20], as modified by Shuen *et al.* [21], and is illustrated in Fig. 2-3.

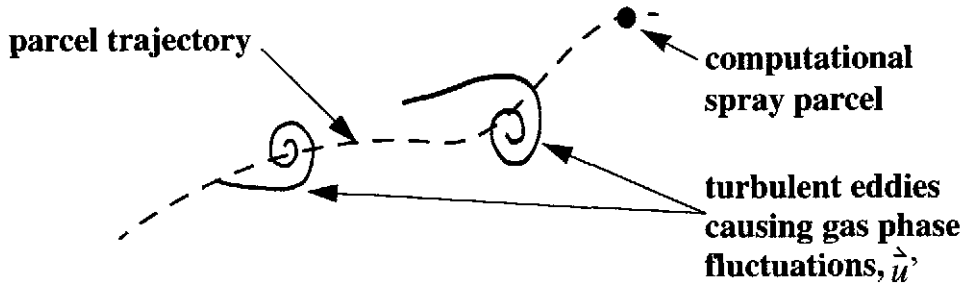

Figure 2-3 Random walk parcel turbulence model.

The model assumes a Gaussian probability density function (PDF) for gas phase fluctuations that are isotropic and parameterized by a zero mean and a variance that is proportional to the kinetic energy,

$$PDF_{u'_{g_j}} = \frac{1}{\sqrt{2\pi\sigma^2}} \exp\left\{-u'_{g_j}/(2\sigma^2)\right\} \tag{2-5}$$

which can be integrated and randomly sampled for each velocity component using the expression,

$$u'_{g_j} = \sqrt{2}\,\sigma\, erf^{-1}(2\,RN - 1) \tag{2-6}$$

where the RMS, σ, is set equal to $\sqrt{2k/3}$ and RN is a random number between 0 and 1. The sampled fluctuating velocities are used to determine one of two outcome events. In the first case, the particle is light enough it will be captured by the turbulent eddy and transported as a fluid particle over a time equal to the eddy lifetime (*i.e.*, $St \ll 1$). In the second case, the particle has sufficient momentum that is will follow a ballistic trajectory and cross the eddy. The total time the particle interacts with the turbulent eddy, τ, is chosen as the minimum time of the eddy lifetime, τ_e, and the particle cross trajectory time, τ_C, using the expressions [21].

$$\begin{aligned} \tau &= MIN(\tau_C, \tau_e) \\ \tau_e &= \sqrt{3/2}\,C_\mu^{3/4} k/\varepsilon \\ \tau_C &= -\tau_d \ln[1 - L_e/(\tau_d |u_{d_j} - u_{g_j}|)] \end{aligned} \tag{2-7}$$

where L_e $(= C_\mu^{3/4} k^{3/2}/\varepsilon)$ is a characteristic turbulent eddy length scale and τ_d $(= 4\rho_g D_d/[3\rho_d C_D |u_{d_j} - u_{g_j}|])$ is the droplet relaxation time (determined from a linearizing Eq. (2-2)).

2.3.2 sub-parcel turbulence model

The effects of unresolved turbulent motions on droplet dispersion within a parcel is based on the group modeling concept of Zhou and Yao [22]. In this model, the sub-parcel distribution of droplets within a parcel is assumed to have a Gaussian distribution as shown in Fig. 2-4,

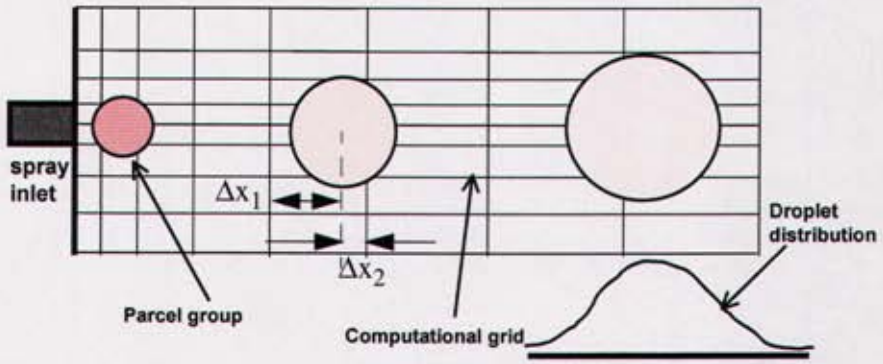

Figure 2-4 Sub-parcel turbulence model.

and can mathematically be expressed as a PDF of droplet distance from the parcel center:

$$PDF_{N_d} = \frac{n_d}{(\sqrt{2\pi})^3 \sigma_x \sigma_y \sigma_z} \exp\left\{-\left(\frac{x^2}{2\sigma_x^2} + \frac{y^2}{2\sigma_y^2} + \frac{z^2}{2\sigma_z^2}\right)\right\} \tag{2-8}$$

where n_d is the total number of droplets in the parcel and x, y and z is the displacement for a droplet from the center of the parcel. The variances, σ_x^2, σ_y^2 and σ_z^2 are the mean square displacements of the droplets from the center of the parcel over a time period, $T = \delta_{t_1} + \delta_{t_2} + \delta_{t_3} + \ldots$, which can be calculated from [22]:

$$\begin{aligned} \sigma_x^2 &= \overline{\delta_{x_1}^2} + \overline{\delta_{x_2}^2} + \overline{\delta_{x_3}^2} + \ldots \\ \sigma_y^2 &= \overline{\delta_{y_1}^2} + \overline{\delta_{y_2}^2} + \overline{\delta_{y_3}^2} + \ldots \\ \sigma_z^2 &= \overline{\delta_{z_1}^2} + \overline{\delta_{z_2}^2} + \overline{\delta_{z_3}^2} + \ldots \end{aligned} \tag{2-9}$$

where δ_x^2, δ_y^2 and δ_z^2 are the mean square displacements over a time interval, δ_{t_i}, and can be calculated from turbulence diffusion theory as [22,23]:

$$\begin{aligned} \overline{\delta_{x_i}^2} &= u'^2_d \delta_{t_i}^2 \\ \overline{\delta_{y_i}^2} &= v'^2_d \delta_{t_i}^2 \\ \overline{\delta_{z_i}^2} &= w'^2_d \delta_{t_i}^2 \end{aligned} \tag{2-10}$$

In Eq. (2-10), u'_{d_j}, are the instantaneous fluctuating parcel velocities that are determined

from transport equations obtained by subtracting an average momentum droplet transport equation from the instantaneous equation of motion resulting in the following [22]:

$$\frac{du'_{d_j}}{dt} = (u'_{g_j} - u'_{d_j})/\tau_d \qquad (2\text{-}11)$$

where u'_{g_j} is the instantaneous fluctuating gas phase velocity determined from Eq. (2-6) and τ_d $(= 4\rho_g D_d/[3\rho_d C_D|u_{d_j} - u_{g_j}|])$ is the droplet relaxation time. The PDF of Eq. (2-8) can be integrated over the CFD grid to determine the number of droplets that lie within a given computational cell, $N_{d_{cell}}$, expressed in terms of error functions,

$$N_{d_{cell}} = \frac{n_d}{8}\prod_{i=1}^{3}[erf(\Delta x_{i_2}/(\sqrt{2}\sigma_i)) - erf(\Delta x_{i_1}/(\sqrt{2}\sigma_i))] \qquad (2\text{-}12)$$

where Δx_{i_1} and Δx_{i_2} are the distances from the parcel center to the lower and upper edges of the computational cell of interest as shown in Fig. 2-4 for one of the three directions.

2.4 Two-way Coupling to the Gas Phase

In order to account for the effects of the spray on the gas phase, source terms are introduced into the gas phase equations. These source terms arise when the conservation equations are phase averaged (see appendix A) and are summarized below in Table 2-1. Source terms are broken into contributions associated with non-evaporating, S_d^*, and evaporating, S_d^{**}, processes. The sum of these two terms is the source term in the gas phase transport equations, $S_d = S_d^* + S_d^{**}$.

Table 2-1 Summary of two-way source terms. Total contribution, Sd=Sd*+Sd.**

Gas Phase Equation	Non-evaporating source terms, Sd*	Evaporating source terms, Sd**
mass	0	$-\frac{1}{V_C}\sum_{n=1}^{N_d}(\dot{m}_d)_n$
momentum	$-\frac{1}{V_C}\sum_{n=1}^{N_d}(F_{D_j})_n$	$-\frac{1}{V_C}\sum_{n=1}^{N_d}(\dot{m}_d u_{d_j})_n$
energy	$-\frac{1}{V_C}\sum_{n=1}^{N_d}(\dot{Q}_c)_n$	$-\frac{1}{V_C}\sum_{n=1}^{N_d}(\dot{m}_d h_g)_n$

2.5 Spray Injector Specification

The parameters which control the spray injection and are summarized in Table 2-3. The variables are read into VULCAN using a FORTRAN namelist format and denoted in the text using a `terminal` text font. The parameters include the location of the injector (`INJP_X`, `INJP_Y` and `INJP_Z`), liquid properties of the spray, and the type of injection method to determine initial drop size (`INJP_Ddis`) and velocity (`INJP_Vdis`).

2.5.1 Drop size

The initial drop sizes are chosen from prescribed PDFs for each injector location. The PDFs can be either a normal (Gaussian), log-normal, Rosin-Rammler or a user specified PDF or JPDF of velocity and diameter. The PDF and cumulative distribution function (CDF) for each of these options are summarized below in Table 2-2 and specified in the code with the FORTRAN namelist variable `INJP_Ddis` (see Table 2-4).

Table 2-2 Summary of drop size PDF/JPDFs used for injection of parcels.

Distribution	PDF/JPDF	CDF
normal/Gaussian	$\frac{1}{\sqrt{2\pi}\sigma_{D_d}}\exp\left[\left(\frac{D_d-\bar{D}_d}{\sqrt{2}\sigma_{D_d}}\right)^2\right]$	$\frac{1}{2}\left[1+erf\left(\frac{D_d-\bar{D}_d}{\sqrt{2}\sigma_{D_d}}\right)\right]$
log-normal	$\frac{1}{\sqrt{2\pi}\sigma_{D_d}D_d}\exp\left[\left(\frac{\ln(D_d/\bar{D}_d)}{\sqrt{2}\sigma D_d}\right)^2\right]$	$\frac{1}{2}\left[1+erf\left(\frac{\ln(D_d/\bar{D}_d)}{\sqrt{2}\sigma D_d}\right)\right]$
Rosin-Rammler	$\frac{qD_d^{(q-1)}}{X^q}\exp\left[-\left(\frac{D_d}{X}\right)^q\right]$	$1-\exp-\left(\frac{D_d}{X}\right)^q$
user-specified distribution with velocity polynomial fits	$\sum_{i=1}^{N_{bins}} W_i[H(D_d-(\Delta D_{d_i})/2)-H(D_d+(\Delta D_{d_i})/2)]$	$\sum_{i=1}^{N_{bins}} W_i\Delta D_{d_i}$
user-specified joint PDF of drop size and velocity	$\sum_{j=1}^{N_{bins}}\sum_{i=1}^{N_{bins}} W_{i,j}[H(D_d-(\Delta D_{d_i})/2)-H(D_d+(\Delta D_{d_i})/2)] \times[H(u_d-(\Delta u_{d_i})/2)-H(u_d+(\Delta u_{d_i})/2)]$	$\sum_{j=1}^{N_{bins}}\sum_{i=1}^{N_{bins}} W_{i,j}\Delta D_{d_i}\Delta u_{d_j}$

The normal and log-normal distributions are parameterized by the first two moments of the PDF, representing the mean, $\bar{D}d$, and RMS, σ_{D_d}, of drop sizes. The first two moments of the Rosin-Rammler distribution are set by the parameters, X, representing some mean parameter, and q, that controls the spread of the distribution and can be related to $\bar{D}d$ and σ_{D_d} by taking

the first and second moments of the PDF.

$$\overline{D_d} = X\Gamma[(1+q)/q]$$
$$\sigma^2_{D_d} = X^2\left\{\Gamma\left(\frac{2+q}{q}\right) - \left[\Gamma\left(\frac{1+q}{q}\right)\right]^2\right\} \quad (2\text{-}13)$$

The user-specified PDF (or JPDF) is prescribed as a discrete sum of specified weight functions, W_i ($W_{i,j}$), for each of the intervals, ΔD_{d_i} (ΔD_{d_i}, Δu_{d_i}), and are mathematically represented by Heaviside functions, H. The user defined droplet size and velocity intervals along with the associated weight functions for those intervals are read in using the FORTRAN namelist variables `INJP_DBINS`, `INJP_VBINS` and `INJP_JPDFDV`, respectively. As an example, Fig. 2-6 shows an example of a user input and associated normalized PDF. Note, user defined weight functions are re-normalized to satisfy the property, $\int P_D dD = 1$ ($\iint P_{D,u} dDdu = 1$).

User input

```
INJP_DBINS(3,1)=1.e-6
INJP_DBINS(3,2)=11.e-6
INJP_DBINS(3,3)=21.e-6
INJP_DBINS(3,4)=31.e-6
INJP_DBINS(3,5)=41.e-6
INJP_DBINS(3,6)=51.e-6
INJP_DBINS(3,7)=61.e-6
INJP_DBINS(3,8)=76.e-6
INJP_DBINS(3,9)=91.e-6
INJP_DBINS(3,10)=106.e-6
INJP_DBINS(3,11)=201.e-6
INJP_JPDFDV(3,1,1)=2094.
INJP_JPDFDV(3,2,1)=7170.
INJP_JPDFDV(3,3,1)=4756.
INJP_JPDFDV(3,4,1)=2869.
INJP_JPDFDV(3,5,1)=1850.
INJP_JPDFDV(3,6,1)=865.
INJP_JPDFDV(3,7,1)=708.
INJP_JPDFDV(3,8,1)=261.
INJP_JPDFDV(3,9,1)=101.
INJP_JPDFDV(3,10,1)=41.
INJP_JPDFDV(3,11,1)=0.
```

Resulting PDF and CDF

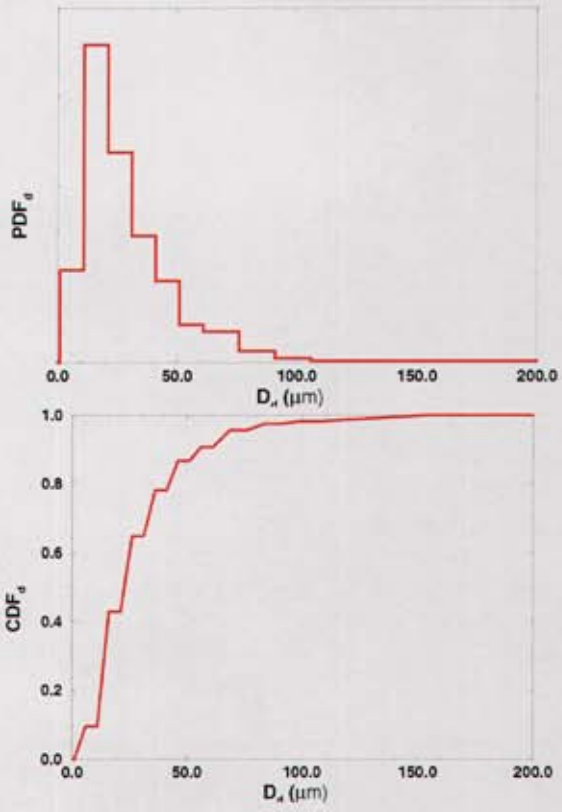

Figure 2-5 User input specification of drop size distribution and resulting PDF and CDF.

2.5.2 Drop velocity

Once the droplet size is determined for each parcel then a parcel velocity is assigned. The spray injection velocity for the droplets can be specified one of four ways: 1) spray angle specification, 2) prescribed velocity in Cartesian coordinates, 3) prescribed velocity in cylindrical coordinates or 4) from a joint probability density function of droplet size and velocity. These velocity injection modes allow for parcels to be injected using data sources ranging from detailed PDPA information (*e.g.*, mass flow rate and the JPDF of drop size and velocity) to less detailed nozzle performance specifications (*e.g.*, mass flow rate and a spray angle). The specification of these different injection options are specified by the `INJP_Vdis` FORTRAN namelist variable (see Tables 2-3 and 2-5).

2.5.2.1 spray angle specification

For this injection method, the magnitude of the parcel velocity is determined by dividing the specified mass flow rate (MFR_{inj}) by the injector cross-sectional area (A_{inj}) and the mass concentration of the parcel (ρ_c), $|u_{d_j}| = MFR_{inj}/(A_{inj}\rho_c)$. Note, if the injector contains only liquid then $\rho_c = \rho_d$. The injection direction of the parcel is determined from the start (α_s) and end (α_e) spray angles using the namelist input variables `INJP_SPANGS` and `INJP_SPANGS`, respectively. Prescribing the spray angle using α_s and α_e allows for droplet distribution patterns that can range from a hollow cone spray (*i.e.*, $\alpha_s \approx \alpha_e$), shown in Fig. 2-6, to a full cone spray (*i.e.*, $\alpha_s = 0$).

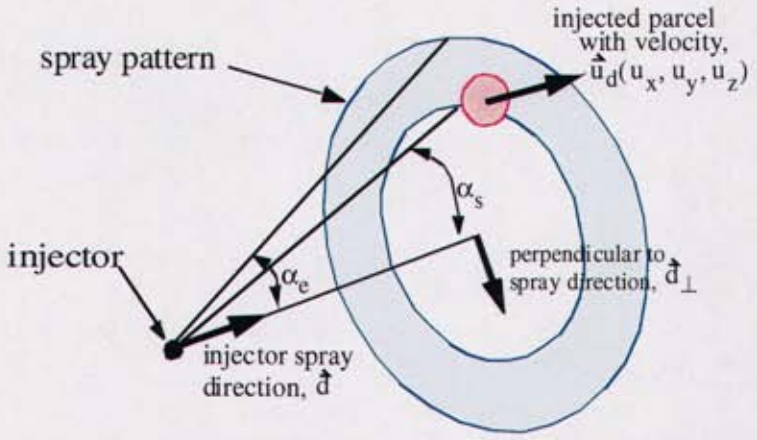

Figure 2-6 Spray injection using a spray angle specification.

The droplets are injected with velocity u_{d_j} into a ring bounded by α_s and α_e using the following relations,

$$u_{d_x} = |u_{d_j}|(d_x + d_{\perp_x})/(|d_j + d_{\perp_j}|)$$
$$u_{d_y} = |u_{d_j}|(d_y + d_{\perp_y})/(|d_j + d_{\perp_j}|) \qquad (2\text{-}14)$$
$$u_{d_z} = |u_{d_j}|(d_z + d_{\perp_z})/(|d_j + d_{\perp_j}|)$$

where d_j is a user specified normalized directional vector for the injector (see Fig. 2-6) and read in using the FORTRAN namelist variables `INJP_dirX`, `INJP_dirY` and `INJP_dirZ` (Note, if a non-normalized directional vector is specified by the user, *i.e.*, $|\overrightarrow{d_\perp}| \neq 1$ then it is automatically normalized). In Eq. (2-14), $d_{\perp_j}$ is a randomly oriented directional vector in the plane perpendicular to d_j and defined by the following coordinate transformation relations:

$$\begin{aligned} d_{\perp_x} &= |d_{\perp_j}|[-\cos(\phi)\sin(\psi) + \sin(\phi)\sin(\theta)\cos(\psi)] \\ d_{\perp_y} &= |d_{\perp_j}|[\cos(\phi)\cos(\psi) + \sin(\phi)\sin(\theta)\sin(\psi)] \\ d_{\perp_z} &= |d_{\perp_j}|[\sin(\phi)\cos(\theta)] \\ |d_{\perp_j}| &= \tan(\alpha_s) + RN_1\ [\tan(\alpha_e) - \tan(\alpha_s)] \end{aligned} \tag{2-15}$$

where RN_1 is a random number between 0 and 1, and the angles θ, ψ and ϕ are defined as:

$$\begin{aligned} \theta &= \text{asin}(-d_z/|d_j|) \\ \psi &= \text{asin}(d_y/[|d_j|\cos(\theta)]) \\ \phi &= 2\pi(RN_2) \end{aligned} \tag{2-16}$$

where RN_2 is another independently chosen random number between 0 and 1. Note, when $RN_1 = 0$ then the drops are injected at an angle α_s and if $RN_1 = 1$ then the drops are injected with angle α_e.

2.5.2.2 prescribed velocity in cartesian coordinates

For this case, the parcel velocities are injected with a given velocity obtained from specified polynomial curve fits of velocity as a function of drop size: $u_{d_j} = \sum_{K=0}^{N_{poly}} a_K D_{d_K}$, where N_{poly} is the order of the polynomial fit and a_K are coefficients specified by the user with the specification of the `INJP_upoly`, `INJP_vpoly` and `INJP_wpoly` namelist variables (see Fig. 2-8 for an example of input). This injection procedure is useful for verification studies where the conditionally averaged droplet velocity on droplet size is measured at locations in the flowfield.

2.5.2.3 prescribed velocity for cylindrical coordinates

This method is similar to the previous case except the polynomial curve fits of droplet velocity are expressed in a cylindrical coordinate system. The components of velocity vector, u_{d_z}, u_{d_R} and u_{d_θ} are specified by the user specified variables `INJP_upoly`, `INJP_vpoly` and `INJP_wpoly` as shown below in Fig. 2-7,

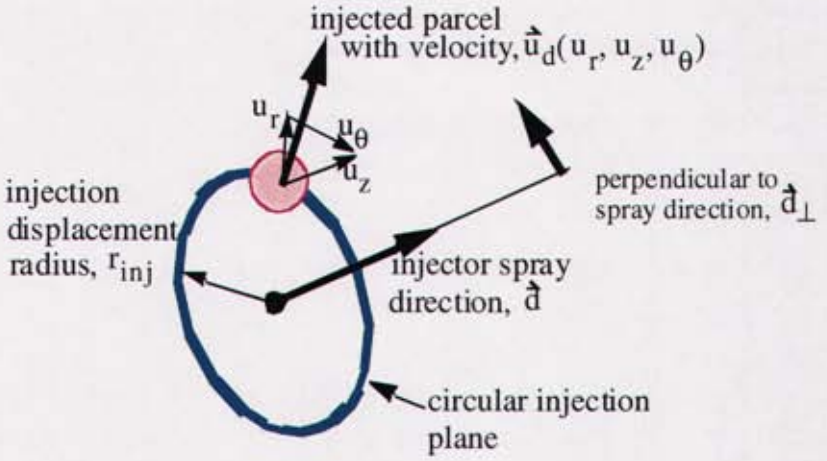

Figure 2-7 Spray injection using polynomial fits for velocity in cylindrical coordinates.

and are used to prescribe a Cartesian velocity for the parcels using the expressions:

$$\begin{aligned} u_{d_x} &= d_x u_{d_z} + d_{\perp_x} u_{d_R} + (d_z d_{\perp_y} - d_y d_{\perp_z}) u_{d_\theta} \\ u_{d_y} &= d_y u_{d_z} + d_{\perp_y} u_{d_R} + (d_z d_{\perp_z} - d_z d_{\perp_x}) u_{d_\theta} \\ u_{d_z} &= d_z u_{d_z} + d_z u_{d_R} + (d_y d_{\perp_x} - d_z d_{\perp_y}) u_{d_\theta} \end{aligned} \qquad (2\text{-}17)$$

where d_j is the user specified directional vector for an injector and $d_{\perp_j}$ is the same as specified in Eq. (2-15). The droplets are injected along in a circle in a plane normal to the injector direction with radius, r_{inj} (`INJP_ rad`), as shown in Fig. 2-7. This parcel injection method is often useful for validation studies of the axisymmetric round sprays when the drop size distribution and conditionally averaged droplet velocities are known as a function of jet radius, as illustrated in Fig. 2-8.

User input for `INJP_upoly`

```
INJP_upoly(1,1)=3.3147623
INJP_upoly(1,2)=199429.398
INJP_upoly(1,3)=-7.04936948e+09
INJP_upoly(1,4)=3.85819672e+13
INJP_upoly(2,1)=2.64192633
INJP_upoly(2,2)=459191.213
INJP_upoly(2,3)=-4.45950052e+09
INJP_upoly(2,4)=7.892235e+12
INJP_upoly(3,1)=4.12972716
INJP_upoly(3,2)=259065.189
INJP_upoly(3,3)=-1.97313203e+09
INJP_upoly(3,4)=4.74792824e+12
```

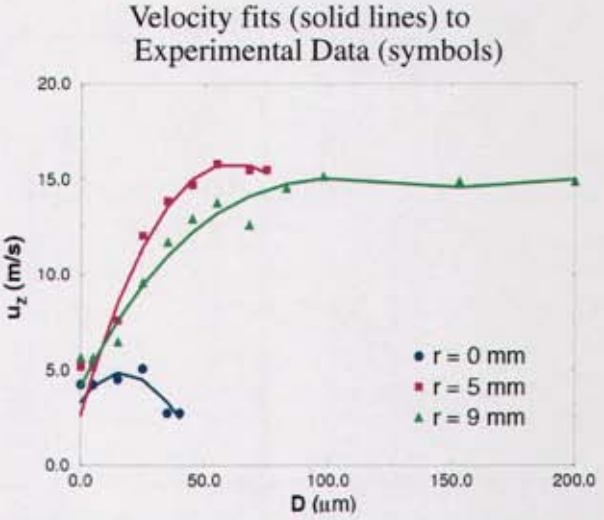

Figure 2-8 Spray injection using polynomial fits for velocity in Cartesian coordinates.

2.5.2.4 prescribed droplet velocity and diameter using a JPDF

In some applications, the joint probability density function (JPDF) of droplet diameter and velocity magnitude are known for a particular spatial location from detailed PDPA experimental measurements. This data may be used for specification of initial droplet size and velocity by sampling from the experimentally derived JPDF. In this case, the velocity magnitude ($|\hat{u}|$) of the injected droplet is specified from the sampling and with direction, d_j.

$$\begin{aligned} u_{d_x} &= d_x|\hat{u}| \\ u_{d_y} &= d_x|\hat{u}| \\ u_{d_z} &= d_x|\hat{u}| \end{aligned} \tag{2-18}$$

The injection location of the droplet may be displaced by a user specified radius (`INJP_rad`) similar to the procedure used for injecting a droplet using the polynomial fits in cylindrical coordinates.

2.6 Droplet Breakup Model

Often in practical spray applications, drop size and velocities are not known sufficiently well for complete specification of the spray model using one of the injection methods discussed in section 2.5. For a plain orifice atomizer (*i.e.*, a liquid jet), phenomenological models are available to predict droplet breakup sizes and velocities. Existing models of droplet breakup include wave breakup model of Reitz *et al.* [26,27], the Taylor Analogy Model (TAB) of O'Rourke and Amsden [28] and extensions [32] and the stochastic spectral relaxation model of Gorokhavski *et al.* [33,34]. The TAB model is adopted in this study. The model assumes a direct analogy between the oscillation of a droplet and a forced spray-mass-damper system as illustrated below in Fig. 2-9.

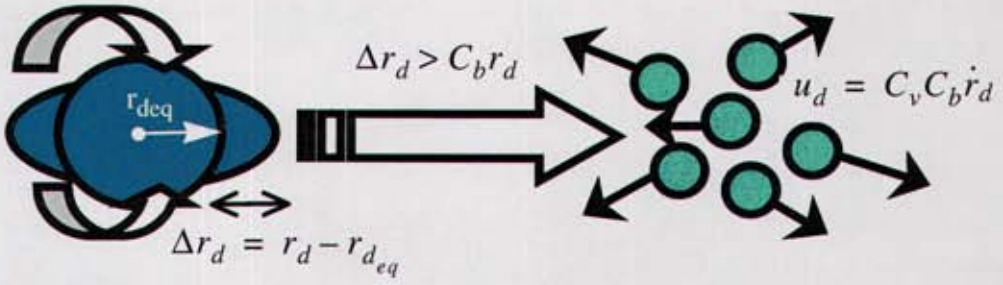

Figure 2-9 Taylor Analogy Breakup model.

This analogy is cast in terms of a second order linear ODE representing the non-dimensional displacement of the droplet radius (Δr_d) from its equilibrium position ($r_{d_{eq}}$), $y = \Delta r_d / r_{d_{eq}}$ [28]:

$$\underbrace{m_d \frac{d^2 y}{dt^2}}_{\text{inertia}} = \underbrace{m_d \frac{C_F}{C_b}\frac{\rho_g}{\rho_l}\frac{|u_{d_j} - u_{g_j}|^2}{r^2}}_{\text{driving force}} - \underbrace{m_d \frac{C_k \sigma}{\rho_l r^3} y}_{\text{spring}} - \underbrace{m_d \frac{C_d \mu_l}{\rho_l r^2}\frac{dy}{dt}}_{\text{damper}} \tag{2-19}$$

where ρ_l, μ_l and σ are the liquid droplet density, molecular viscosity and surface tension, respectively. The model constants C_F, C_b, C_k and C_d are calibrated using a combination of theoretical considerations of droplet oscillation frequencies and experimental data leading to the values of 1/3, 1/2, 8 and 5, respectively [25]. Both y and $\dot{y}$ are updated and stored for each parcel during the course of a simulation. The analytical solution to Eq. (2-19) is that of a simple harmonic oscillator where y and $\dot{y}$ at time t are advanced to $t + \Delta t$ using the following relations [25].

$$y(t+\Delta t) = \frac{We}{C} + \left\{\left(y(t) - \frac{We}{C}\right)\cos(\omega\Delta t) + \frac{1}{\omega}\left(\dot{y}(t) + \frac{y(t) - We/C}{\tau_b}\right)\sin(\omega\Delta t)\right\}\exp(-\Delta t/\tau_b) \qquad (2\text{-}20)$$

$$\dot{y}(t+\Delta t) = \frac{\frac{We}{C} - y(t)}{\tau_b} + \left\{\frac{1}{\omega}\left(\dot{y}(t) + \frac{y(t) - We/C}{\tau_b}\right)\cos(\omega\Delta t) - \left(y(t) - \frac{We}{C}\right)\sin(\omega\Delta t)\right\}\omega\exp(-\Delta t/\tau_b) \qquad (2\text{-}21)$$

In Eqs. (2-20) and (2-21), C $(= C_k C_b / C_f = 12)$ is a grouping of the TAB modeling constants, τ_b $(= 2\rho_l r^2/(C_d \mu_l))$ is a droplet oscillation relaxation time, and ω $(= \sqrt{C_k\sigma/(\rho_l r^3) - (1/\tau_b)^2})$ is the droplet oscillation frequency.

The implementation details of Eqs. (2-20) and (2-21) is provided in Ref. [25] and expanded on here for additional clarity. The numerical procedure consists of first calculating the value of ω. For very small drops, $\omega^2 < 0$ and distortions in the drop are negligible. For this case, $y(t+\Delta t)$ and $\dot{y}(t+\Delta t)$ are simply set equal to zero. When $\omega^2 > 0$, then the oscillation amplitude of the undamped oscillation is first determined using the relation: $A = \sqrt{(y(t) - We/C)^2 + (\dot{y}(t)/\omega)^2}$ (*i.e.*, assume $\tau_b \to \infty$ and the add the squares of the factors in front of the sine and cosine terms of Eq. (2-20)). If $A + We/C < 1$, then the amplitude of the disturbance can not cause droplet breakup over a time period, $t + \Delta t$ (*i.e.*, set $y(t+\Delta t) = 1$ in Eq. (2-20), allow $\tau_b \to \infty$, and then combine sine and cosine terms into a single cosine term with phase, Φ, as: $y(t+\Delta t) = We/C + A\cos(\omega\Delta t + \Phi)$). In this case, Eqs. (2-20) and (2-21) are used to update the values of y and $\dot{y}$ for the current time step. If $A + We/C > 1$, then breakup is possible and the breakup time, t_{bu}, is determined from solving for the smallest root of the equation: $We/C + A\cos(|\omega\Delta t + \Phi|) = 1$, where Φ is determined from the relations: $\cos(\Phi) = (y(t) - We/C)/A$ and $\sin(\Phi) = -\dot{y}(t)/(A\omega)$ [25]. If $\Delta t < t_{bu}$, then no breakup occurs and y and $\dot{y}$ are updated. If $t_{bu} < \Delta t$ then breakup occurs, as illustrated in Fig. 2-9, with the size and number of the newly formed drops determined from mass and energy conservation principles [28].

$$r_d(t+\Delta t) = r_d(t)/\left[1 + \frac{8K}{20} + \frac{\rho_l r(t)^3}{\sigma}\frac{6K-5}{120}y^2\right] \qquad (2\text{-}22)$$

$$n_d(t+\Delta t) = [r_d(t)/r_d(t+\Delta t)]^3$$

The model constant K in Eq. (2-22) represents the ratio of the total energy in the distorted droplet to the droplet oscillation energy in the fundamental mode and takes on a value of 10/3 [28].

The velocity of the new drops are set to that of the parent drop plus a breakup velocity component normal to the parent droplet trajectory, $u_{\perp_j}$, with magnitude $|u_{\perp_j}| = (C_v C_b r(t)\dot{y} D_d)/2$ and a direction chosen randomly in a plane normal to the path of the parent drop.

$$\begin{aligned} u_{\perp x} &= |u_{\perp_j}|[-\cos(\phi)\sin(\psi) + \sin(\phi)\sin(\theta)\cos(\psi)] \\ u_{\perp y} &= |u_{\perp_j}|[\cos(\phi)\cos(\psi) + \sin(\phi)\sin(\theta)\sin(\psi)] \\ u_{\perp z} &= |u_{\perp_j}|[\sin(\phi)\cos(\theta)] \end{aligned} \tag{2-23}$$

The angles θ $(= \text{asin}(-u_{d_z}/|u_{d_j}|))$, and ψ $(= (\text{asin}(u_{d_y}/|u_{d_j}|))/\cos(\theta))$ are expressed in terms of the velocities of the parent drop and the angle $\phi(= 2\pi RN)$ is a random angle in the plane perpendicular to the parent drop trajectory having a value between 0 and 2π. After breakup, y and $\dot{y}$ of the newly formed droplets are initialized to zero where they may grow and eventually breakup again if the We numbers of the new droplets are sufficiently large.

2.7 Droplet-Droplet Collision Model

Droplet-droplet collisions often occur during the atomization of a liquid jet. For some applications, accounting for these collisions may be important in reproducing observed mean drop sizes downstream of primary atomization. The collision model used in this work is adapted from the work of O'Rourke [35]. This approach only accounts for either droplet-droplet bouncing or coalescence and not droplet-droplet shattering effects which may become important at higher impact velocities [36]. Collisions of pairs of computational parcels are treated using a statistical process description. The procedure starts by checking to see if two parcels occupy the same computational cell. If they do not share the same cell, then it is assumed that collisions cannot occur. If they do share the same cell, then the parcel containing the larger drops are designated as the collectors and parcel containing the smaller drops designated as the donors. The expected frequency of collisions between one collector and all the donor droplets is assumed to obey a Poisson process with frequency parameter λ having the following function form.

$$\lambda = |u_{d_1 1} - u_{d_j 2}|\pi(r_{d_1} - r_{d_2})^2 \frac{n_{d1}}{V_C} \tag{2-24}$$

The subscripts "1" and "2" represent the properties associated with the parcel containing the donors and collectors, respectively, and V_C is the volume of the computational cell. For a Poisson process, the likelihood that a collector undergoes n collisions is defined with the fol-

lowing probability density function (PDF) distribution,

$$PDF_{coll}(n) = \frac{e^{-\bar{n}}(\bar{n})^n}{n!} \tag{2-25}$$

where $\bar{n}$ is the average number of collisions per unit time, Δt, and is related to the frequency parameter using the relation, $\bar{n} = \lambda \Delta t$. Setting $n = 0$ in Eq. (2-25) we can see that the probability of no collisions over the time period Δt is $e^{-\bar{n}}$. The Poisson PDF is sampled by choosing a random number, RN_1, that lies between 0 and 1. If $RN_1 < e^{-\bar{n}}$, then no collisions occur for that particular droplet-collector pair. If $RN_1 > e^{-\bar{n}}$, then it assumed that *all* the collector drops in parcel "2" undergo collision with the donor droplets of parcel "1". The model outcome of the collision is based on the experimental and theoretical work of Brazier-Smith *et al.* [37] concerning the collision of water droplets. In the Brazier-Smith study, three regimes of droplet collision behavior are identified and found to be dependent on an impact parameter, b, defined as the perpendicular distance between the center of one drop and the undeflected trajectory of the other [37] (see Fig. 2-5). These impact regimes consist of 1) grazing collisions with satellite drops, 2) grazing collisions without satellite drops and 3) complete coalescence. The collision model of O'Rourke only accounts for grazing droplet impacts and coalescence events without satellite drop formation.

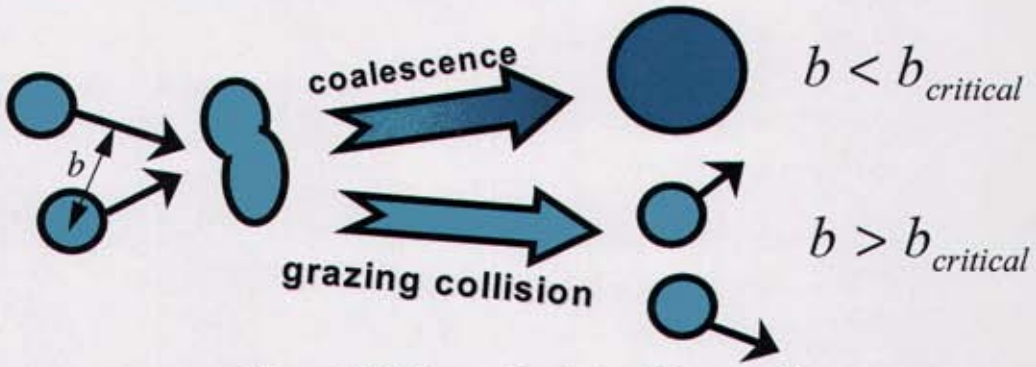

Figure 2-10 Spray droplet collision model.

The model assumes that at impact if b is less than some threshold value, $b_{critical}$, then the drops will coalescence, otherwise a grazing collision event is assumed to occur. Since individual droplets are not tracked in the code, but rather clouds of drops, then the exact position of the drops are not known. The value of b for every droplet-droplet impact therefore can not be directly calculated, and instead, a statistical description is devised. In this approach, a coalescence efficiency is first defined, $\varepsilon_{coal} \equiv (b_{critical}/(r_{d_1} + r_{d_2}))^2$ and determined by a curve fit of the experimental data of Brazier-Smith [35] leading to the following relation:

$$\varepsilon_{coal} = min\left[2.4f(\gamma_r)\frac{1}{We}, 1\right] \tag{2-26}$$

where $f(\gamma_r)(=\gamma_r^3 - 2.4\gamma_r^2 + 2.7\gamma_r)$ is a function of the ratio of collector to donor droplet radi, γ_r, and We is a critical impact Weber number defined as: $We = (\rho_l |u_{d_i1} - u_{d_j2}|^2 r_{d_1})/\sigma$. The outcome of the droplet-droplet collision is determined by first choosing an additional random number, $0 < RN_2 < 1$, representing a sampling of the coalescence efficiency. A corresponding impact parameter is then determined using the definition of the coalescence efficiency parameter: $b = \sqrt{RN_2}(r_{d_1} + r_{d_2})$. If $b < b_{critical}$, then the collision results in a coalescence otherwise a grazing collision is assumed. Once the outcome of the collision is known, then the number of collisions that occur are determined by finding the value of n for which the following inequality is satisfied.

$$\sum_{k=0}^{n-1} PDF_{coll}(k) < RN_1 \leq \sum_{k=0}^{n} PDF_{coll}(k) \tag{2-27}$$

Once the type of collision and the number of drops for the collision are determined, then properties of collector and donor parcels are updated based on mass, momentum and energy principles for which the details can be found in refs. [25] and [35]. These relations are summarized below for first a collision event resulting in coalescence,

$$\begin{aligned} u_{d_{j2}}' &= (u_{d_{j2}} m_{d_2} + u_{d_{j1}} m_{d_1} n)/m_{d_{tot}} \\ T_{d_2}' &= (T_{d_2} m_{d_2} + T_{d_1} m_{d_1} n)/m_{d_{tot}} \\ m_{d_2}' &= m_{d_2} + m_{d_1} n = m_{d_{tot}} \\ D_{d_2}' &= [6 m_{d_{tot}}/(\pi \rho_{l_2})]^{1/3} \\ n_{d_1}' &= n_{d_1} - n \end{aligned} \tag{2-28}$$

where the primed quantities and $m_{d_{tot}}$ denote parcel properties and total mass of the collector droplet after collision, *i.e.*, $m_{d_{tot}} = n m_{d_1} + m_{d_2}$. Note, if $n n_{d_2} > n_{d_1}$ then there are physically not enough drops in the donor droplet parcel to accommodate all of the collisions with the drops in the collector parcel. In this case, n is reset to n_{d_1}/n_{d_2} and the mass of the drops associated with the droplet parcel are set equal to zero and eventually removed from the calculation.

In a grazing collision event, only momentum exchange is considered since the time scales associated with heat exchange are much longer then the collision event. For this case, if $n_{d_2} > n_{d_1}$ then droplet velocities after collision are set as follows [35]:

$$\begin{aligned} u_{d_{j1}}' &= \frac{m_{d_1} u_{d_{j1}} + m_{d_2} u_{d_{j2}} + m_{d_2}(u_{d_{j1}} - u_{d_{j2}})\left[\dfrac{b - b_{critical}}{r_{d_1} + r_{d_2} - b_{critical}}\right]}{m_{d_1} + m_{d_2}} \\ u_{d_{j2}}' &= \frac{n_{d_1} u_{d_{j2}} + (n_{d_2} - n_{d_1}) u_{d_{j2}}}{n_{d_2}} \end{aligned} \tag{2-29}$$

otherwise $n_{d_1} > n_{d_2}$ and the droplet velocities are given as [35]:

$$u_{d_{j2}}' = \frac{m_{d_1}u_{d_{j1}} + m_{d_2}u_{d_{j2}} + m_{d_1}(u_{d_{j2}} - u_{d_{j1}})\left[\frac{b - b_{critical}}{r_{d_1} + r_{d_2} - b_{critical}}\right]}{m_{d_1} + m_{d_2}}$$

$$u_{d_{j1}}' = \frac{n_{d_2}u_{d_{j1}} + (n_{d_1} - n_{d_2})u_{d_{j1}}}{n_{d_1}} \tag{2-30}$$

It should be emphasized that the collision model of O'Rourke is based solely on the interaction of water drops and so is only appropriate for use on water spray suppression applications. Use of this model for other liquids such as hydrocarbon fuels is not recommended without first modification of the impact regime criterion [29-31].

2.8 Droplet Boundary Conditions

When a drop passes through an open boundary of the computational domain, the mass of the particle is set to a small value and then eliminated by the re-ordering procedure that occurs at the start of each spray sub-cycling routine.

If the drop approaches a solid boundary of the domain, then a simple hard sphere model is used to determine the trajectory of the drop after it impacts the surface using the following expressions:

$$u_{d_n}' = -R_n u_{d_n}$$
$$u_{d_t}' = R_t u_{d_t} \tag{2-31}$$

where the primes are the velocity after impact with the wall and the subscript "n" and "t" denote the normal and tangential velocity components of the droplet with respect to the wall. The quantities R_n and R_t are user specified coefficients of restitution.

This boundary condition treatment is fairly crude. Advanced models would account for more realistic droplet bounce as well as account for droplet shattering and adhesion to the solid surface. The inclusion of these more advanced boundary condition treatments will be the focus of future efforts to be discussed in Chapter 5

2.9 Spray Statistics

During a spray simulation, data is gathered for post-processing and statistical analysis. Both Eulerian and Lagrangian statistical quantities are collected for making comparisons to experiments and for engineering analysis. This type of information is particularly useful for a statistically stationary flows for which higher order statistical information, such as droplet dispersion, are useful for code verification and validation checks. Note, the spray model is currently set up for collecting quantities over a single simulation so time averaged quantities may be calculated. A capability for collecting ensemble statistics by re-running simulations has not yet been incorporated into the model, however, for statistically stationary flows, time

averaging and ensemble averaging are equivalent since the processes are ergodic.

2.9.1 Eulerian statistics

Eulerian statistics is information gathered at a specified location in the flow. The sum and sum of the squares of droplet and gas phase properties are stored and updated at user prescribed time intervals during a simulation for later post-processing. This information is used at the end of the run to determined mean ($\overline{(\ldots)}$) and root mean square (RMS) ($\sigma_{(\ldots)}$) of droplet and gas properties at every grid point in the domain using the following relations:

$$\begin{aligned}
\overline{\phi_d} &= \sum \phi_d / N_d \\
\sigma_{\phi_d} &= \left[\left(\sum \phi_d^2 - \left(\sum \phi_d\right)^2\right)/\mathrm{N}_d\right]^{1/2} \\
\overline{\phi_g} &= \sum \phi_g / N \\
\sigma_{\phi_g} &= \left[\left(\sum \phi_g^2 - \left(\sum \phi_g\right)^2\right)/N\right]^{1/2}
\end{aligned} \tag{2-32}$$

where $\langle\phi\rangle_d$, σ_{ϕ_d} and $\langle\phi\rangle_g$, σ_{ϕ_g} are the mean and RMS of the droplet and gas phase properties, respectively. The parameter N is the total number of flowfield realizations or "snapshots" taken at user specified time intervals, `(dtpstat)`. The variable, N_d, represents the total number of drops and is equal to the sum of droplets per parcel over all parcels and over all realizations, *i.e.*, $N_d = \sum_N \sum_{N_P} n_d$.

2.9.2 Conditional Eulerian statistics

In addition to mean and RMS droplet statistics for all drops, information for conditional statistics is also gathered during a simulation for later post-processing. These statistics provide mean and RMS information on droplet properties binned according to drop size. These statistics are calculated in the same way as the ensemble mean and RMS except the sums are grouped into bins corresponding to different size drop diameters. Conditional statistics are especially useful when comparing model predictions to phase doppler particle anemometry (PDPA) measurements of droplet size and velocity.

2.9.3 Lagrangian statistics

Data required to calculate Lagrangian dispersion statistics can also be gathered during the simulation. Lagrangian dispersion statistics provide information on the mean droplet spatial displacement over a given time interval. The Lagrangian dispersion statistics are calculated using:

$$\langle x_i^2 \rangle(\tau) = \left(\sum [x_i(\tau) - x_i(\tau = 0)]^2\right)/N_d \tag{2-33}$$

where τ is the time over which a parcel has travelled to position, $x_i(\tau)$, from a user prescribed reference position, $x_i(\tau = 0)$, that is user specified using the `dstatsXpos`, `dstatsYpos`, `dstatsZpos`, `dstatstol` and `dstatstime` input parameters.

Table 2-3 Summary of input parameters for spray injector.

Namelist Variable	Parameter Description
ninjec	Number of spray injection locations
INJP_LABEL(i)	Name of fuel for the i^{th} injector.
INJP_X(i)	X-location of i^{th} injector. [m]
INJP_Y(i)	Y-location of i^{th} injector. [m]
INJP_Z(i)	Z-location of i^{th} injector. [m]
INJP_PPIMIN(i)	Number of parcels injected at the i^{th} injector.
INJP_PPPMIN(i)	Min no. of particles per parcel for the i^{th} injector.
INJP_PPPMAX(i)	Max no. of particles per parcel for the i^{th} injector.
INJP_MFR(i)	Mass flow rate of the i^{th} injector. [kg/s]
INJP_AREA(i)	Cross-sectional area of the i^{th} injector. [m^2]
INJP_DENp(i)	Density of the fluid for the i^{th} injector. [kg/m^3]
INJP_CONp(i)	Concentration of paricles for the i^{th} injector (*i.e.*, INJP_CONp(i)=INJP_DENp(i) for a pure fluid). [kg/m^3]
INJP_SPRANGS(i)	Start of spray angle for the i^{th} injector. [degrees]
INJP_SPRANGSE(i)	End of spray angle for the i^{th} injector. [degrees]
INJP_dirX(i)	X-direction of the spray for the i^{th} injector.
INJP_dirY(i)	Y-direction of the spray for the i^{th} injector.
INJP_dirZ(i)	Z-direction of the spray for the i^{th} injector.
INJP_rad(i)	Radius of the injection for the i^{th} injector. [m]
INJP_Ddis(i)	Type of droplet diameter selection for the i^{th} injector.
INJP_Vdis(i)	Type of droplet velocity selection for the i^{th} injector.
INJP_aveDp(i)	Average droplet diameter for the i^{th} injector. [m]
INJP_rmsDp(i)	RMS of droplet diameter for the i^{th} injector. [m]
INJP_Tp(i)	Initial droplet diameter temperature for the i^{th} injector. [K]
INJP_MWp(i)	Molecular weight of liquid for the i^{th} injector. [kg/gmol]

Table 2-3 Summary of input parameters for spray injector.

Namelist Variable	Parameter Description
INJP_Clp(i)	Specific heat of liquid for the i^{th} injector. [J/kg-K]
INJP_Emp(i)	Surface emissivity of liquid for the i^{th} injector.
INJP_Scf(i)	Droplet film Schmidt number for the i^{th} injector.
INJP_Prf(i)	Droplet film Prandtl number of the i^{th} injector.
INJP_Prefvapp(i)	Reference saturation pressure for the liquid from the i^{th} injector. [Pa]
INJP_Trefvapp(i)	Reference saturation temperature for the liquid from the i^{th} injector. [K]
INJP_Hvaprefp(i)	Reference heat of vaporization for liquid from the i^{th} injector. [J/kg-K]
INJP_Tlcp(i)	Critical temperature of the liquid from the i^{th} injector. [K]
INJP_Dminp(i)	Minimum droplet size from the i^{th} injector. [m]
INJP_TABflag(i)	Toggle for the breakup model for droplets coming from the i^{th} injector.
INJP_TAByp(i)	Initialization of y for the TAB model used for drops from the i^{th} injector.
INJP_TABydotp(i)	Initialization of $\dot{y}$ for the TAB model used for drops from the i^{th} injector.
INJP_COLLflag(i)	Toggle the droplet-droplet collsion model for drops coming from the i^{th} injector.
INJP_STp(i)	Surface tension of liquid from the i^{th} injector. [kg/m-s]
INJP_mup(i)	Molecular viscosity of the liquid from the i^{th} injector. [kg-m/s]
INJP_axp(i)	X-body force acceleration on drops from the i^{th} injector. [m/s^2]
INJP_ayp(i)	Y-body force acceleration on drops from the i^{th} injector. [m/s^2]
INJP_azp(i)	Z-body force acceleration on drops from the i^{th} injector. [m/s^2]

Table 2-4 Summary of injection modes for droplet size.

INJP_Ddis options	Type of Droplet Size Distribution
1	Normal
2	Log-Normal
3	Rosin-Rammler
4	User defined PDF for Drop size
5	User defined JPDF for drop size and velocity

Table 2-5 Summary of injection modes for droplet velocity.

INJP_Vdis options	Type of Droplet Velocity Specification
1	spray angle specification
2	User defined velocity in Cartesian coordinates using drop size dependent polynomial fits
3	User defined velocity in cylindrical coordinates using drop size dependent polynomial fits
4	User defined using JPDF for drop size and velocity

CHAPTER 3 NUMERICAL IMPLEMENTATION

Table 3-1 lists the timing control parameters for activation of the spray model. Input parameters, `tpinjecs`, `tpsnaps` and `tpstats` define starting times for injection of droplets, storing of Tecplot plot files, and the start time for data collection needed for later statistical analysis, respectively. The control variables `dtpinjecs`, `dtpsnaps` and `dtpstats` define the time intervals of these events. The `dtpinjecs` and `dtpsnaps` parameters can be modified midway through a simulation by specifying `tpinjecs` and `tpsnaps` to times that are earlier than the current simulation time. The `dtpstats` parameter can only be changed if statistical data collection has not been initiated.

The remaining control parameters (`dtclipfac`, `dtsubcycmin`, `MSfrac`, `ESfrac` and `USfrac`) are associated with two-way coupling to the gas phase. These parameters are discussed in more detail in section 3.3 on numerical sub-cycling. The following subsections provide detail on numerical integration of the droplet equations, interpolation of gas-phase properties, and coupling the spray source terms listed in Table 2-1 with the gas-phase transport equations.

3.1 Integration of Droplet Equations

The system of ODE's for droplet transport are numerically stiff when the droplet is undergoing rapid evaporation and if the diameter becomes too small (i.e., $D_d \leq 1\mu m$). Use of standard explicit integration techniques for these cases will result in numerical instabilities. To avoid this problem, the *LSODE* (Lawerence Livermore solver for ODE's) library [38] is used to integrate the droplet equations. This solver is specifically designed for integration of numerically stiff sets of ODE's for which the details can be found in Ref. [38]. In addition to the LSODE library, a fourth order Runge-Kutta scheme [39] is also implemented for use for problems involving larger drops, (*i.e.*, $D_d > 100\mu m$) undergoing little mass evaporation.

3.2 Interpolation of Gas Phase Properties

Interpolation of gas phase properties from the CFD grid are needed for integration of the droplet transport equations. High order Lagrange interpolating polynomials [39] are incorporated for this purpose. The algorithm is devised so that an arbitrarily high order interpolation stencil may be employed with stencil shifting near boundaries to maintain formal accuracy. However for most applications, the order of the stencil is usually set to first order (linear) to be consistent with the convection discretization error in VULCAN.

3.3 Coupling of Droplet Source Terms into Gas Phase

The time scales associated with droplet evaporation are on the order of microseconds while the time scales of convection are on the order of milliseconds or larger. This large disparity in time scales can introduce numerical stability when the liquid and gas phases are coupled. For rapidly evaporating sprays and high mass loadings, simply integrating the gas-phase transport equations using the spray source terms will lead to at best nonphysical results, and at worst, numerical instability. Two different approaches may be used to mitigate this problem. The first is to solve the droplet and gas-phase equations using a fully implicit algorithm. This

would require several trial integrations of the parcels over a given time step until local convergence is achieved. The disadvantage of such a scheme is the excessive expensive re-integrating a large number of computational parcels and it is not pursued in this study. Alternatively, an explicit operator splitting procedure, similar to the work of Amsden *et al.* [40], is adopted to achieve tight coupling between the gas and liquid phase systems. In this approach, the convection and diffusion processes are frozen while the spray source terms are sub-cycled to update the gas phase mass, momentum and energy transport equations. After sub-cycling, the gas-phase transport equations are then updated by convection and diffusion processes using the SIMPLE algorithm. The time interval for sub-cycling is determined dynamically from estimates of the maximum mass, momentum and heat exchange that can occur over a given time step, Δt:

$$\begin{aligned} \Delta Mass_{max} &= \rho_g(Y_g - \overline{Y_{f_d}}) \\ \Delta Mom_{max} &= \rho_g(U_{i_g} - \overline{u_{d_j}}) \\ \Delta Energy_{max} &= \rho_g C_{p_g}(T_g - \overline{T_{d_f}}) \end{aligned} \tag{3-1}$$

where $\overline{Y_{f_d}}$, $\overline{T_{f_d}}$ and $\overline{u_{d_j}}$ are the local average droplet film mass fraction temperature and droplet velocity in a computational cell. The sub-cycling time step is chosen to allow for only a user-specified fraction (`MSfrac`, `ESfrac` and `USfrac`) of the current maximum to be exchanged over a given time step using the following relation:

$$\Delta t_{subcyc} = MIN\begin{cases} \texttt{MSfrac}\,(\Delta Mass_{max}/Sd_M^{**}) \\ \texttt{USfrac}\,(\Delta Mom_{max}/Sd_{U_j}^{*}) \\ \texttt{ESfrac}\,(\Delta Energy_{max}/Sd_E^{*}) \end{cases} \tag{3-2}$$

where Sd_M^{**}, $Sd_{U_j}^{*}$ and Sd_E^{*} are the spray source terms for mass, the contribution to momentum due to droplet drag and the contribution to energy due to convection heat transfer as defined in Table 2-1. For some applications, the physical sub-cycling time step is much too small to be computationally practical and is restricted to values that are greater than a user specified value (`dtsubcycmin`).

The sub-cycling algorithm estimates a future time step from the current spray source terms collected over the previous sub-cycling time step. Occasionally, this procedure will not respond quickly enough to a a sudden jump in the spray source term due to short lived transients leading to non-physical results. This may occur in situations for which the physical time scales are very small, such as during the first few time steps of a rapidly evaporating spray, or when a future sub-cycling time step is determined to be smaller than `dtsubcycmin`. For these special cases, the future sub-cycling time step is correctly estimated to be very small, indicating that the current time step is much too large. Rather than resetting the position of the parcels and re-integrating them at a smaller time step, the source terms are simply clipped as follows:

$$S_d = S_d\ MIN\,[1, \texttt{dtclipfac}\,(\Delta t_{subcyc}(new)/\Delta t_{subcyc}(old))] \tag{3-3}$$

where `dtclipfac` is a user specified sub-cycling clipping factor that controls the degree of clipping. Numerical testing of the sub-cycling indicates that reasonable values for `dtclipfac` are between 1 and approximately 10. If `dtclipfac` is set equal to 1, then the source terms are clipped every time Δt_{subcyc} is reduced. If `dtclipfac` is set equal to 10, then the source terms are rarely ever clipped but will lead to numerical instability or non-physical results if a sudden transient event is encountered. Trial and error suggests that a value of 5 for `dtclipfac` allows for reasonable solution of the coupled gas-liquid transport equations over a wide range of flow conditions.

Table 3-1 Summary of spray model control input parameters

Namelist Variable	Parameter Description
`tpinjecs`	Start time for injection of spray(s) (s)
`tpsnaps`	Start time for taking graphical data dumps of the gas and liquid flow (s)
`tpstats`	Start time for taking data for statistics (s)
`dtpsnap`	Time interval between graphical data dumps (s)
`dtinjec`	Time interval between parcel injection (s)
`dtpstat`	Time interval between sampling for statistics (s)
`dtclipfac`	Clipping factor for two-way coupling ~ 5 (1 < `dtclipfac < 10`)
`dtsubcycmin`	Absolute minimum time interval for sub-cycling
`MSfrac`	Mass gas-phase source term sub-cycling parameter ~ 0.1 (0 < `MSfrac < 1`)
`ESfrac`	Energy gas-phase source term sub-cycling parameter ~ 0.5 (0 < `ESfrac < 1`)
`USfrac`	Momentum gas-phase source term sub-cycling parameter ~ 0.1 (0 < `USfrac < 1`)

CHAPTER 4 RESULTS

The scales for which mass, momentum and energy transfer from the liquid droplets to the gas phase are often order of magnitudes smaller then the mesh used for the gas phase computation. As a result, much of the droplet-gas phase interactions are modelled using empirically based models that have been described in the previous sections. To build confidence in the predictive capability of these models, a verification and validation (V&V) effort is planned and summarized below in Table 4-1.

Table 4-1 Summary of verification and validation problems

V&V Problem	Motivation
non-evaporating falling drop (analytical solution)	assess transport algorithm and drag model
evaporating drop with uniform flow (analytical solution)	assess mass and heat evaporative and thin-skin film property models
particle dispersion in grid generated turbulence (analytical solution, Snyder and Lumley, [41] and Wells and Stock [42], Chen and Faeth [43])	assess turbulence models for uniform sized particle with prescribed turbulence (*i.e.*, prescribe values for k and ε
particle dispersion in turbulent round jet (Yuu *et al.*, [48])	assess turbulence models for uniform sized drops with solved turbulence (*i.e.*, solve for k and ε using transport equations)
non-reacting non-evaporating spray (Skaggs *et al.* [55])	assess turbulence models for non-uniform drops with two-way momentum coupling effects
non-reacting, evaporating spray (Skaggs *et al.* [55], McDonell *et al.* [51])	assess droplet transport, evaporation, turbulence coupling
combusting fuel spray (Skaggs *et al.* [55], McDonell *et al.* [52], Widmann *et al.*[53])	assess droplet transport, evaporation, turbulence, gas-phase combustion model coupling
spray suppression using liquid agent (Sheinson *et al.* [56])	assess droplet transport, evaporation, turbulence, gas-phase combustion and gas-phase suppression model coupling

The table is arranged so that the physical complexity of the problem increases with descend-

ing order through the table, with the first row being the simplest and the last entry being the most difficult. The first three tests allow for simple verification of the droplet transport algorithm, evaporation model and turbulence models for which analytical solutions are available. The last five rows of the table are validation problems for which data is available from well-controlled experiments. The focus of the future work using the spray model is to run these problems and ascertain the predictive capability of the VULCAN spray model for application to the live-fire problem. Effort has already been started in performing V&V assessments of the spray model. The following sections provide additional details of the cases listed in Table 4-1, and presentation of results where work has already begun.

4.1 Falling Particles

For the special case of a free falling single particle in air, a terminal velocity is reached due to the balance of gravity forces with the drag on the sphere. In this limiting case, the terminal velocity can be determined by solving for u_d in the following non-linear equation,

$$u_d^2 = \frac{4\rho_d D_d}{3\rho_g C_D} g \tag{4-1}$$

where C_D is given by Eq. 2-3. The particle types are chosen to be the same as those used in the experiments of Snyder and Lumley [41]. The VULCAN simulations are conducted by injecting a single particle into a quiescent flow and allowing for the solution of the droplet transport equations until the particle achieves a terminal velocity. A comparison of the terminal velocity using Eq. (4-1) and using VULCAN for several particle sizes are summarized below in Table 4-2.

Table 4-2 Summary of droplet terminal velocity verification problem.

Particle Properties (taken from Ref. [41])	Terminal velocity (cm/s) (analytical result using Eq. (4-1), with $\rho_g = 1.184$ and $\mu_g = 2.1622\times10^{-5}$)	Terminal velocity (cm/s) (VULCAN numerical result, with $\rho_g = 1.184$ and $\mu_g = 2.1622\times10^{-5}$)
hollow glass $D_d = 46.5\mu m$ $\rho_d = 0.26 g/cm^3$	1.3920	1.3920
solid glass $D_d = 87\mu m$ $\rho_d = 2.5 g/cm^3$	38.2042	38.2042
corn pollen $D_d = 87\mu m$ $\rho_d = 1.0 g/cm^3$	16.6908	16.6908

Particle Properties (taken from Ref. [41])	Terminal velocity (cm/s) (analytical result using Eq. (4-1), with ρ_g = 1.184 and $\mu_g = 2.1622\times10^{-5}$)	Terminal velocity (cm/s) (VULCAN numerical result, with ρ_g = 1.184 and $\mu_g = 2.1622\times10^{-5}$)
copper $D_d = 46.5\mu m$ $\rho_d = 8.9 g/cm^3$	41.3686	41.3686

A comparison of the terminal velocities indicate that the VULCAN predictions match the analytical result within at least single-precision error tolerances. This relatively simple verification check provides confidence that the transport equations for droplet momentum and use of the LSODE library and drag model are correctly coded.

4.2 Single Evaporating Drop

This V&V problem is designed to assess the evaporative heat and mass and droplet film property models described in sections 2.1 and 2.2. The problem is to examine the transient response of a single droplet suddenly exposed to a uniform velocity field. The results from the numerical study will be compared to detailed single droplet numerical solutions and experimental measurements of this problem taken from the open literature [12,54]. In addition, analytical solutions of the steady-state behavior of the droplet mass evaporation rate can be derived [19] (*i.e.*, the "D_d^2 law") and compared to the steady-state VULCAN droplet solution.

4.3 Particle Dispersion in Turbulent Flows

In this section, the droplet turbulence models, described in section 2.3, are tested. Two model problems are chosen. The first is particle dispersion in grid generated turbulence experiments of Snyder and Lumley [41]. The experiment best approximates the conditions for homogeneous turbulence allowing for VULCAN predictions to be compared to both experimental data as well as theoretical predictions based on consideration of turbulence theory for the dispersion of fluid-marker particles [23]. The turbulence input parameters to the spray turbulence models, k and ε, are known directly from experimental measurements and used directly rather than being solved. This prevents the inaccuracies of using the standard $k-\varepsilon$ model clouding the assessment of the spray turbulence models. The second model problem is the dispersion of fly ash in a turbulent air jet measured by Yuu *et al.* [48]. This experiment allows for the additional complexity of non-homogeneous turbulence to be introduced for which the $k-\varepsilon$ turbulence model is used and shown to produce reasonable results.

4.3.1 grid generated turbulence

The conditions for the Snyder and Lumley experiment [41] consists of releasing four different particle types downstream of grid generated turbulence in a wind tunnel and measuring the Lagrangian dispersion displacement statistics or each case. The particles used were hol-

low glass, corn pollen, solid glass and copper and their properties are summarized in table 4-2. The turbulent kinetic energy and its dissipation were measured in the experiment and can be described using the empirically derived expressions [46]:

$$k = \frac{\bar{U}^2}{2}\left[\frac{1}{42.4(x/M-16)} + \frac{2}{39.4(x/M-12)}\right]$$
$$\varepsilon = \frac{\bar{U}^3}{2M}\left[\frac{1}{42.4(x/M-16)^2} + \frac{2}{39.4(x/M-12)^2}\right] \qquad (4\text{-}2)$$

where $\bar{U} = 6.55\ m/s$ is the mean flow speed in the tunnel and $M = 1''$ is the mesh spacing of the grid. Figure 4-1 shows the Lagrangian particle dispersion from the experiment and the prediction from VULCAN using Eqs.(4-2) for k and ε. Also on the plot is the analytical result from MacInnes and Bracco [44] for particle dispersion of a fluid-marker particle in homogeneous turbulence using Taylor's hypothesis for the random walk turbulence model of section 2.3.1.

$$\bar{y}^2 = \begin{cases} \overline{u'^2}t^2[1 - t/(3\tau_e)] & \text{for} \quad 0 \le \tau \le \tau_e \\ \overline{u'^2}\tau_e[t - \tau_e/3] & \text{for} \quad \tau > \tau_e \end{cases} \qquad (4\text{-}3)$$

The time scale, τ_e $(= \sqrt{3/2}C_\mu^{3/4}k/\varepsilon)$ is the large eddy turn over time and is assumed constant for homogenous turbulence. The k and ε taken from the experiment for this expression are $0.2626 m^2/s^2$ and $12.542 m^2/s^3$ and corresponds to the first measurement location of $x/M = 20$. This curve (marked with an **X**) can be thought of as the maximum possible dispersion that the random walk turbulence model can predict for this problem. In the other extreme a completely deterministic solution approach without any random walk turbulence model of particle transport would result in the particle dispersion being identically zero.

The analytical result using Eq. (4-3) and the VULCAN marker particle prediction are almost identical for all time with a slight 4% maximum error at 400 *msec* providing a high level of confidence that the random walk droplet turbulence model is properly coded. The small differences in particle dispersion for numerical predictions of the analytical result as well as the appearance of the slightly higher values of dispersion for the hollow glass and corn pollen cases than the theoretical maximum may be attributed to statistical error due to the finite number of realizations taken (20,000) and will be further investigated in future studies.

Comparing the results experimental measurements to the VULCAN predication indicates that the model does well for the heavier particles were cross-trajectory effects are predominant. However, for the lighter particles the model under-predicts the dispersion for the hollow glass case and over-predicts for the corn pollen case when the particles are more likely to follow the flow field. The difficulties of predicting the dispersion of these very light particles (*i.e.*, low Stokes number) are consistent with previous studies using the same model and more sophisticated droplet turbulent dispersion models have been proposed [44-47]. These models

come at an additional computational cost and since the application of the spray model will primarily be focused on transport of relatively large liquid drops (*i.e.*, $D_d > 50\mu m$), the current turbulence model is sufficient since it appears to work well in that limit.

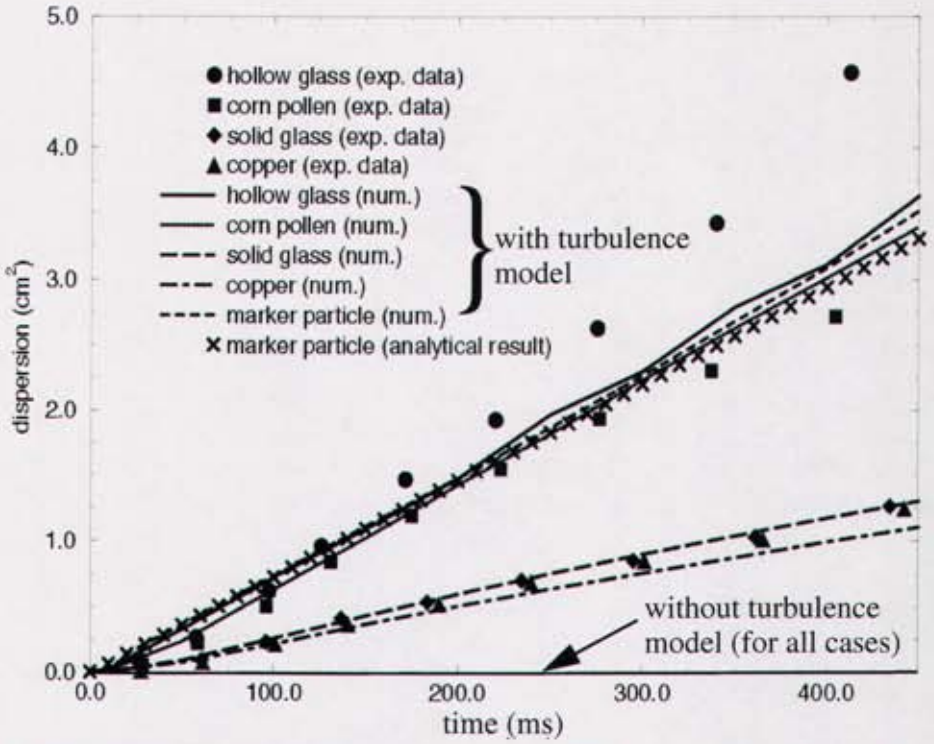

Figure 4-1 Lagrangian particle dispersion from grid generated turbulence. Symbols •, ■, ♦, ▲ are experimental results from Ref. [41], lines are numerical predictions and the X symbol is an analytical result using Eq. (4-3) for homogenous turbulence.

4.3.2 turbulent round jet

The second set of validation problems used to test the droplet turbulence models are the experiments of Yuu *et al.* [48] concerning the dispersion of 20 μm fly ash particles from a fully developed turbulent round jet. The experimental setup consists of a mixture of air and fly ash emitting out of an 8 *mm* diameter orifice for which several cases were examined with various air velocity and mass loadings. Two cases are selected to compare against and the experimental conditions are summarized in the table below.

Table 4-3 Summary of experimental conditions of Yuu *et al.* [48].

	U_{gas} (m/s)	U_{part} (m/s)	particle concentration (g/m^3)	$\dot{m}_{part}$ (mg/s)	loading ratio $(\dot{m}_{part}/\dot{m}_{gas})$
Case 1	100	54	0.8	2.17	0.00043
Case 2	20	14	4.0	2.82	0.0028

Comparisons of the numerical predictions using VULCAN to the experimental data (as reduced by Shuen *et al.* [49]) for these two cases are shown in Figs. 4-2 and 4-3.

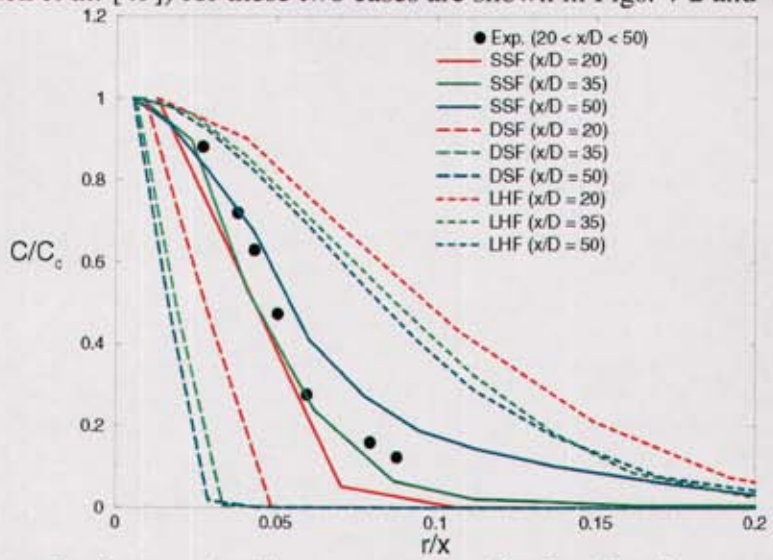

Figure 4-2 Normalized concentration versus normalized radius for case 1. Symbols are experimental data and lines are numerical predictions using LHF, DSF and SSF modeling approximations.

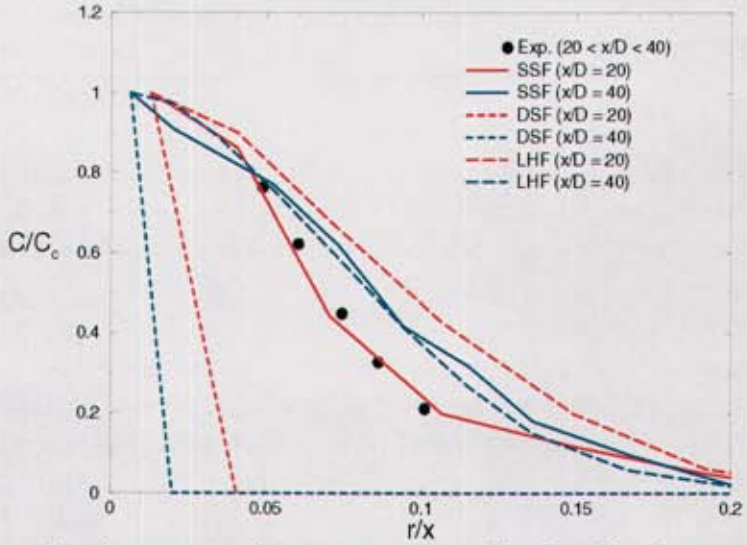

Figure 4-3 Normalized concentration versus normalized radius for case 2. Symbols are experimental data and lines are numerical predictions using LHF, DSF and SSF modeling approximations.

In these comparisons, three spray modeling methodologies are explored. In the first approach, the particles are treated as a continuous media for which the concentration of the particles are related to the transport of a passive scalar. Or in other words, the spray is transported as a gas with the equivalent mass loading. This approximation has been termed as the locally homogenous flow (LHF) approximation [9] and is valid in the limit of very fine parti-

cles where the local Stokes number of the particle are always much less than one. Employing this approximation for cases 1 and 2 shows that the use of a LHF approximation results in a large over prediction of the spread rate for both cases 1 and 2. The agreement is better for case 2 than case 1 due to reduced effects of slip allowing for a better approximation of the LHF limit.

The second spray modeling approach is based on a deterministic separated flow (DSF) approach for which the effects of subgrid turbulence are neglected [9]. In all cases, the spread rate of the particle concentration is severely under predicted indicating that the particles follow a more ballistic trajectory. Lastly, in the cases where the use of a turbulence model is employed in the stochastic separated flow (SSF) approximation, the prediction of particle concentration profiles are in reasonably good agreement with the experimental data. These results indicated that even for relatively simple particle laden flows it is important to account for the effects of subgrid turbulence and the need for a turbulence model in the spray transport.

4.4 Non-evaporating Sprays

The purpose of the non-evaporating spray experiments is to test the spray model where there is a spectrum of drop sizes to keep track of without the added complexities of droplet evaporation and combustion processes. Surprisingly, there is only limited experimental data in the literature on well-controlled experiments appropriate for model validation for this relatively simple case. This part of the spray modeling effort will be in close collaboration with the Army Research Labs (ARL) to define and compare the predictions of the VULCAN spray model with detailed experimental measurements of water sprays using phase doppler particle anemometry (PDPA) [55]. Specifically, the study will help to address or provide guidance to the following questions.

1. Which of the boundary conditions for the spray injector discussed in section 2.5 is sufficient for matching with a PDPA measurement?
2. How many measurement locations are necessary to completely define a downstream measurement plane to account for all of the liquid mass flux?
3. Given the initial conditions of the joint probability density function (JPDF) of droplet size and velocity from a PDPA measurement, can the spray model predict the subsequent down stream development of the JPDF?
4. Is is possible to modify the droplet breakup and collision models to predict the drop size and velocity JPDF distributions for simple atomizers?

4.5 Evaporating sprays

The step to evaporating sprays introduces the unknown of whether the simple evaporation model used for a single droplet is also applicable to a large group of drops. The modeling again will be in close collaboration with the experimental program at ARL using diesel sprays. The results of this effort will help to address or provide guidance to the following questions.

1. How important are subgrid spatial variations in mass fraction to the group evaporation

from a collection of drops?
2. If local fluctuations in species and temperature are important, then can a local turbulent mixing can be formulated to account for these effects analogous to the random walk model used for particle dispersion?

4.6 Combusting Sprays

Some limited published data on combusting sprays are available from McDonald and Samulson [51,52] and Widmann *et al.* [53]. Numerical simulations of VULCAN for these cases along with the collaborative work with ARL will provide the necessary information to provide some level of assessment as to the utility of the current spray model for application to the live-fire problem. Some of the outstanding issues for these cases are summarized below.

1. Are group combustion (see Refs. [79-81]) effects important? If so, how to extend the current modeling methodology to accommodate some of those concepts?
2. How important are the effects of radiation transport heat transfer to pre-vaporization of the spray before it is advected into a combusting region?
3. What are the effects of solid blockage on droplet size due to impact as well as on the combustion event?

4.7 Combusting Sprays and/or Pool Fire with Spray Suppression

The most complicated problem scenario for the use of the two-phase spray model is when both the fire source and the suppression agent are in a liquid phase. The most likely scenarios are a fuel spray or fuel spill fire and a liquid fire suppressant is released. The specific issues to be addressed are summarized below.

1. What are the effects of water dilution in modeling fire suppression of pool fires using water sprays or mists? How to account for these effects?
2. Is it important to account for droplet-droplet interactions between a fuel spray and a liquid suppressant? If so, how to properly model these events?
3. How important is it to account for thermal radiation in vaporizing a liquid fire suppressant before it reaches the flame zones?

Preliminary work in this area has been initiated using the data being collected at the Naval Research Laboratory (NRL) Chesapeake Bay Detachment Facility [56]. The details of this study are provided in the following section for a case study on assessing the sensitivities of fire suppression to spray nozzle configurations.

Case Study: Fire Suppression in Enclosures

Current research in Halon alternatives for aircraft dry bays indicates that new suppression agents have higher boiling temperatures (*i.e.*, $T_b > 330K$) and will most likely be released in partially liquid state. One of the agents currently being considered for shipboard applications is the use of water mist and water spray technologies. Preliminary work has been taken in assessing the utility of the spray model for water spray suppression. The specific application

for this work is water spray of an enclosed pool fire currently being tested at the Naval Research Laboratory (NRL) Chesapeake Bay facility. A sketch of the NRL test facility is shown in Figure 4-4. The facility is ventilated using one inlet port located near the top of the enclosure and two exit ports that are located on the opposite corner. The volumetic flow rate is maintained at 7.1 m^3/s allowing for one air exchange every four minutes. A 0.305 m (12") square pool of heptane is simulated through constant mass flux boundary conditions at the bottom of the domain. The mass flux is chosen as $\dot{m}" = 0.0288 kg/(m^2 - s)$ based on empirical correlations from Drysdale [57] (*i.e.*, $\dot{m}" = \dot{m}"_\infty(1 - \exp(-k\beta D))$) where for heptane $\dot{m}"_\infty = 0.101$ and $k\beta = 1.1$) resulting in a 123 kW fire. In attempt to reproduce conditions from existing experimental procedures at the facility, a constant mass flow condition is imposed on the inlet boundary while a constant pressure condition is used at the outflow boundaries. After 45 s, a constant pressure condition is imposed on both the inlet and outlet boundaries to simulate deactivation of the ventilation system. Two spray configurations, representative of the systems being explored at NRL, are considered in this study and are illustrated in Figure 4-5. The first consists of a single high pressure spray nozzle located at the center top of the enclosure while the second uses four lower pressure nozzles that cover each quadrant of the cell. Unfortunately, the exact drop size and velocity distributions, as well as the spray distribution pattern, are not well known and could not be obtained from the system manufacturers. Based on estimates of the operating pressures and atomizer cross sectional areas, the same mass flow rate, 0.53 kg/s, was determined for both systems and droplet velocities of 166 and 83 m/s for configuration 1 and 2, respectively were calculated. The spray injection is modeled as a solid cone spray that randomly injects computational parcels to cover the specified solid angle. The spray angles (α) are computed to allow for a spray to reach the corners of the room in configuration 1 or a cell quadrant in configuration 2 as if the droplet were to follow an outermost trajectory and are set equal to 35.3° and 19.5°, respectively. Lastly, four different drop size classes of D_d = 25, 75, 150 and 300 μm are used for each configuration to explore the sensitivity of drop size and cover the range of plausible drop sizes expected in the experiments.

The VULCAN simulations presented here employ a 34 x 30 x 37 grid to discretize a cubical enclosure with a length of 3.05 m (10 ft) on a side. The simulations are first performed for 8600 time steps to simulate 45 s of physical time to account for a typical preburn time for a fire to ignite and develop. The calculations are then advanced another 3500 time steps to allow for simulation of 10 s of physical time to elapse with the water suppression activated. During the transient period of spray injection, a total of 33,000 computational parcels are injected into the domain with approximately 2000 parcels at any given time in the simulation.

Figure 4-6 (a) shows the volume averaged gas temperature for the lower half (*i.e.*, Z < 1.5 m), <Tl>, upper half (*i.e.*, Z > 1.5m), <Tu>, and for the entire domain, <T>, during the preburn part of the simulation. As shown, <Tu>, rapidly increases by approximately 100K in the first 30 s of the preburn as the hot gases from the pool fire collect near the ceiling of the enclosure. After 30 s, all temperature averages appear to increase approximately linearly at the same rate of 2 K/sec.

Figure 4-6 (b) shows temperature isocontours with velocity vectors superimposed for a cross section through the domain after the preburn period. At this time, the flow shows large vortical flow structures that entrain air due to the periodic varicose puffing mode of the pool fire. In addition, the location of the peak temperature is shifted toward the outflow boundary resulting in the high temperature gases flowing on average along the ceiling to the exit boundary on the opposite wall.

After the preburn time, the water spray is injected forming a jet of entrained hot gas near the ceiling as the local air is transported by droplet drag and directed downward. Figure 4-7 shows instantaneous predictions of the gas phase velocity at the spray injection planes along with location and velocity of the droplets after 0.4 s of spray injection using 150μm droplets for (a) configuration 1 and (b) configuration 2. The maximum magnitude of the gas phase velocity for configuration 2 is approximately 15 m/s and is about half the peak value of 30 m/s for configuration 2. This difference is due to the lower mass flow and associated lower droplet injection velocities for the lower pressure four-nozzle system in configuration 2.

Figure 4-8 presents volume averaged temperatures after the start of spray injection for configuration 1 using all four drop size classes showing (a) <Tl> and (b) <Tu>. In Figure 4-8 (a), the largest, 300 μm drops show an initial increase in temperature for the first 2.5 s after injection. This surprising increase in temperature is due to the enhanced turbulent mixing of the jet and advection on the pool surface before enough water has evaporated to start to cool the flow near the base of the fire. This prediction is consistent with previous observations of Atreya *et al.* on the use of water sprays [58]. In contrast, the injection of the 25 μm drops results in a sudden drop of 40 K in the average temperature near the base of the fire in the first second, leveling off for another 3 s and then suddenly decreasing again. This temperature history can be attributed to the transient jet development. A high concentration of small droplets are located at the leading edge of the jet offering effective suppression of the pool fire for a short (1 second) period followed by enhanced turbulent mixing that slows the suppression until the initial jet transient has passed at 48 sec. The intermediate, 75 and 150 μm, cases also show signs of the transient jet development with some short lived reduction in temperature due to initial injection of drops followed by an increase in temperature and then a more gradual decrease. Figure 4-8 (b) shows <Tu> time history and indicates that, in general, the smaller droplets allow for more effective suppression than larger drops with the 25 and 75 μm providing almost same initial reduction in <Tu> for the first 4.5 s after injection.

Figure 4-9 show (a) <Tl> and (b) <Tu> time history for the second spray system configuration. In this case, the enhanced turbulent mixing due to the starting jet from the sprays is not as pronounced as in configuration 1 due to the lower injection velocities of the droplets and the spatial offset of the spray injection locations relative to the position of the pool fire. The decrease in turbulent mixing, along with the longer residence time of droplets to interact with the fire, allows for the spray in configuration 2 to decrease the <Tu> temperature more quickly than in configuration 1 as shown by comparing Figure 4-9 (b) to Figure 4-8 (b). In addition, both Figure 4-9 (a) and (b) indicate an optimum drop size exists between 25 and 75 μm that is sufficiently large to penetrate the high temperature fire plume, yet be small enough

to be an effective suppressant at the flame zones. This observation is consistent with the previous water spray suppression studies of pool fires [59].

In summary, a spray model applicable to simulating the effects of water mist on large scale pool fires has been developed and applied to a practical fire scenario representative of experiments at NRL. The findings from this study indicate a strong sensitivity of fire suppression to initial drop size where injection of larger drops may actually cause an increase in overall temperature due to enhanced turbulent mixing before enough spray can evaporate to provide sufficient cooling. In spray configuration 2, an optimum drop size was observed indicating that nozzles that generate very fine mist (*i.e.*, $D_d < 50$ μm) will not always provide maximum suppression for these conditions. Lastly, within the assumptions imposed for the inlet spray conditions and the fire scenario studied, the spray configuration using several lower pressure nozzles appeared to be slightly more effective at decreasing the gas phase temperature shortly after spray injection than a single high pressure nozzle.

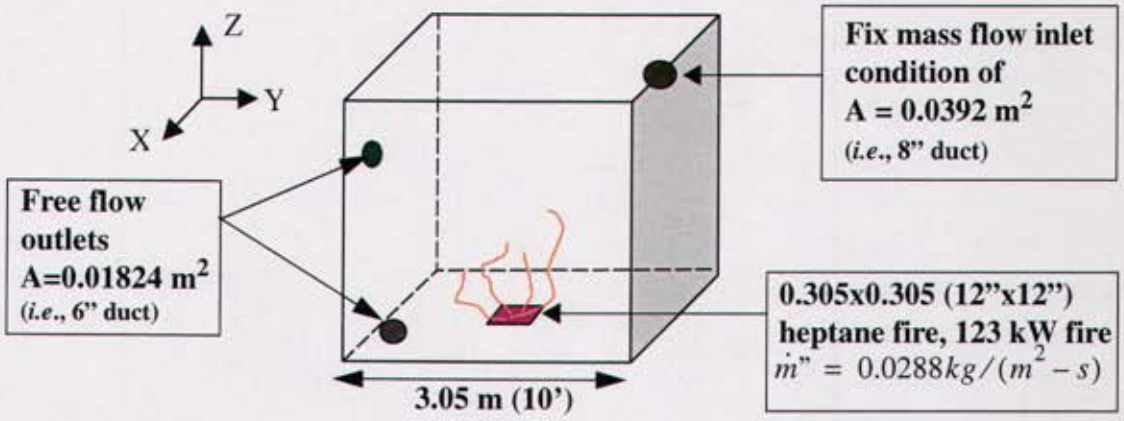

Figure 4-4 Schematic of NRL facility

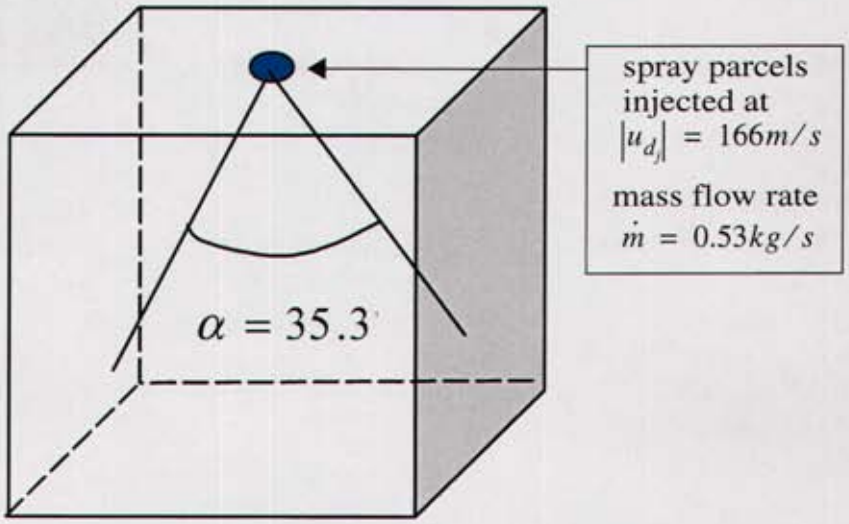

(a)

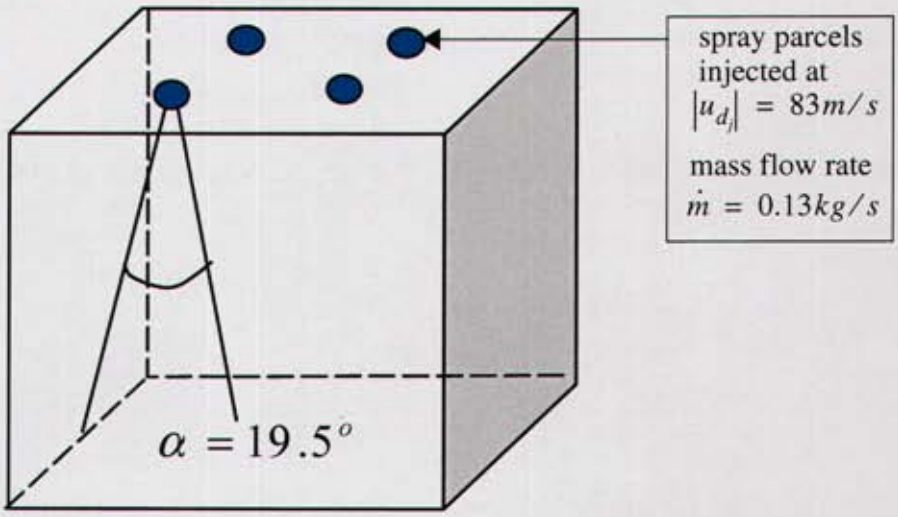

(b)

Figure 4-5 Schematic of spray system configurations using (a) one single high pressure nozzle (configuration 1) and (b) quadrant approach using four lower pressure nozzles (configuration 2).

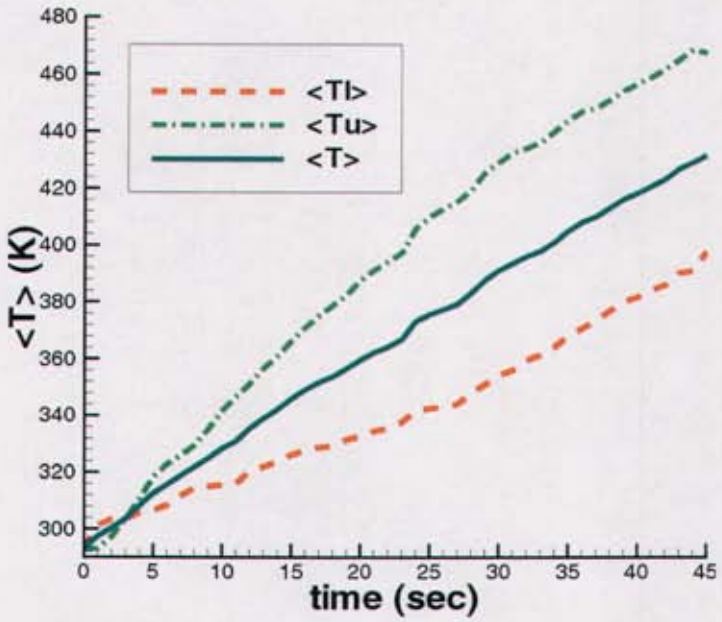

(a)

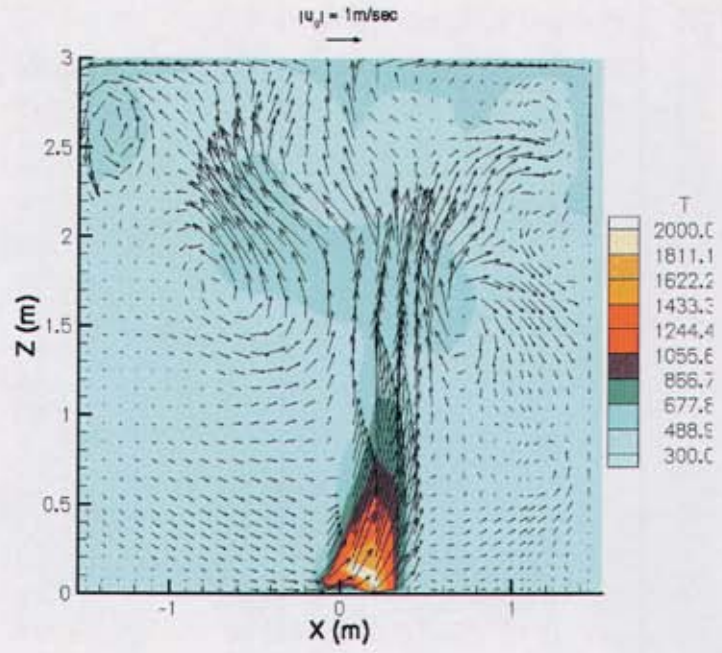

(b)

Figure 4-6 Temperature variations during preburn showing (a) volumetric average temperature versus time and (b) instantaneous snapshot of temperature isocontour slice through center of cell (*i.e.*, y=0) with superimposed velocity vectors at 45 seconds.

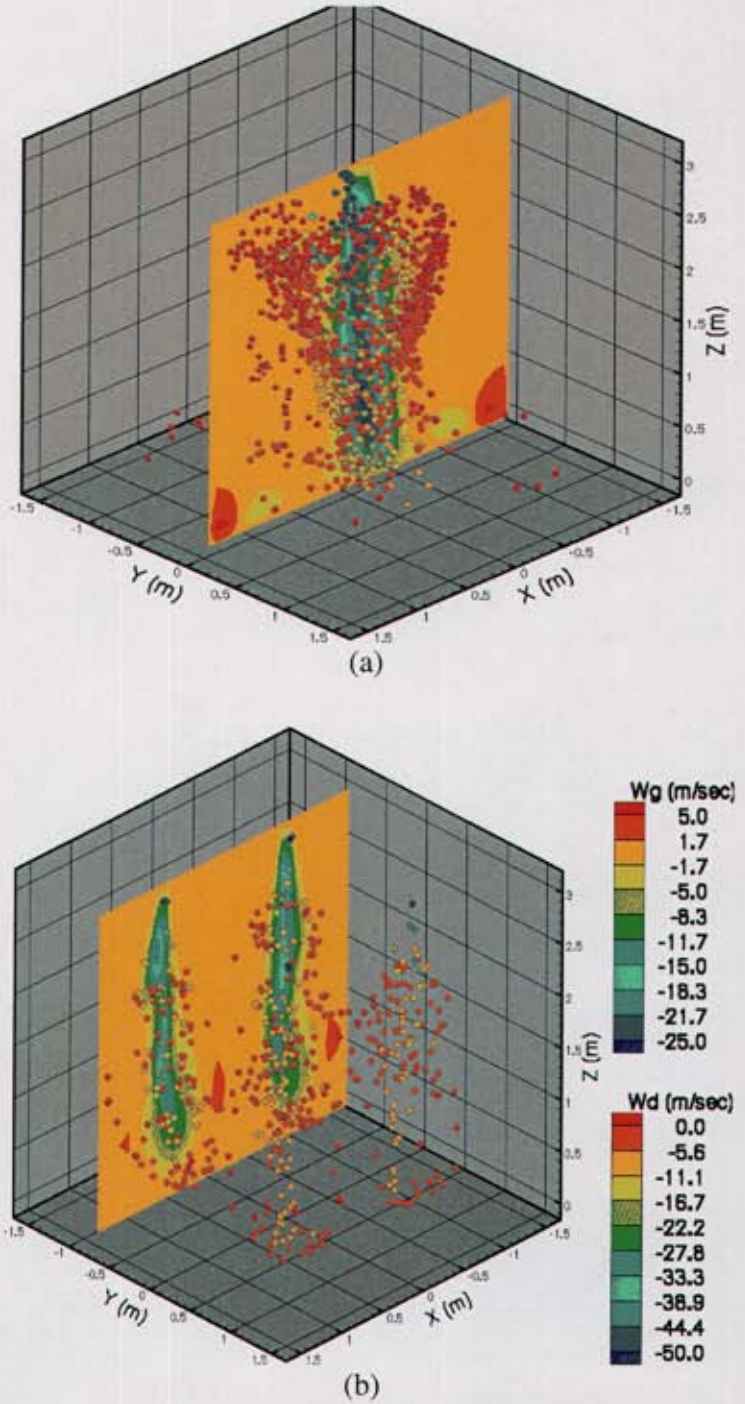

Figure 4-7 Instantaneous snapshot of water spray suppression 0.4 s after injection showing isocontours of gas and droplet phase vertical velocity at plane of injection for (a) spray configuration 1 (contour slice at y=0.0 m) and (b) spray configuration 2 (contour slice at y=-0.8 m).

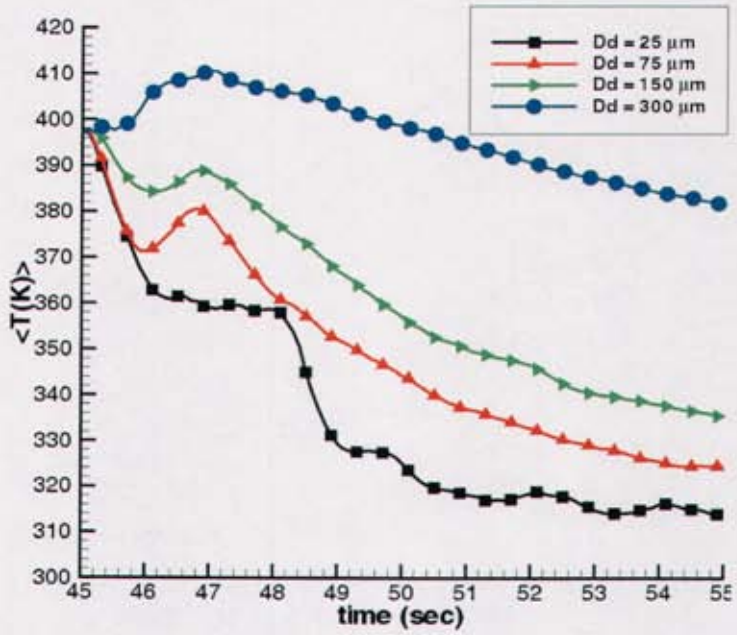

(a)

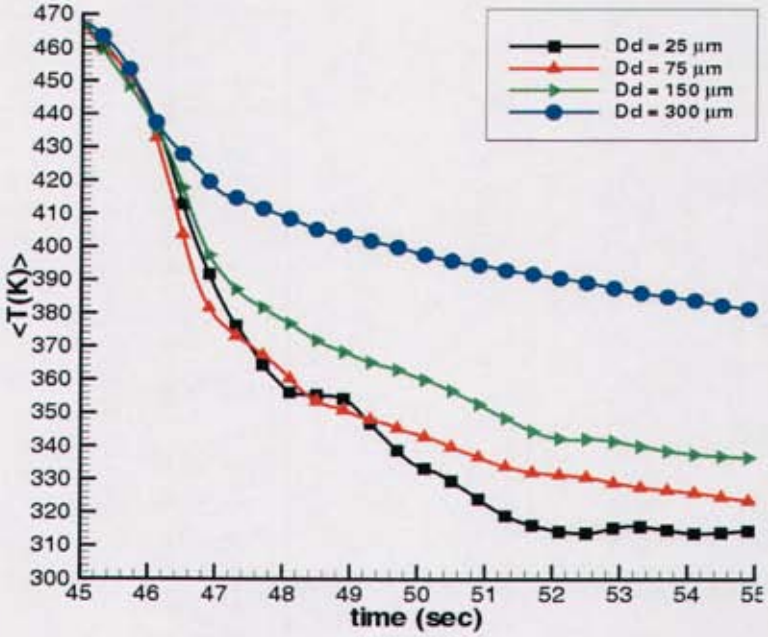

(b)

Figure 4-8 Volume averaged temperature for configuration 1 showing (a) <Tl> and (b) <Tu> verses time.

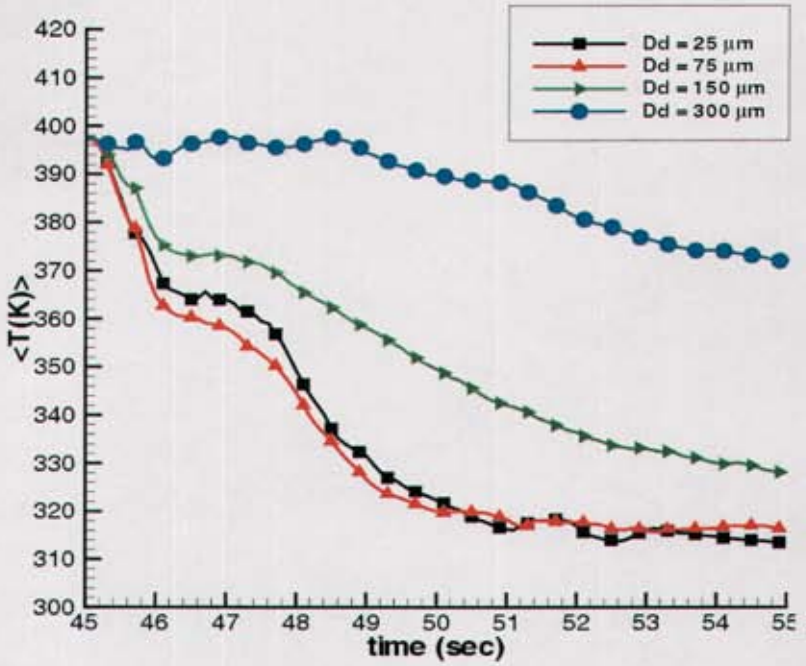

(a)

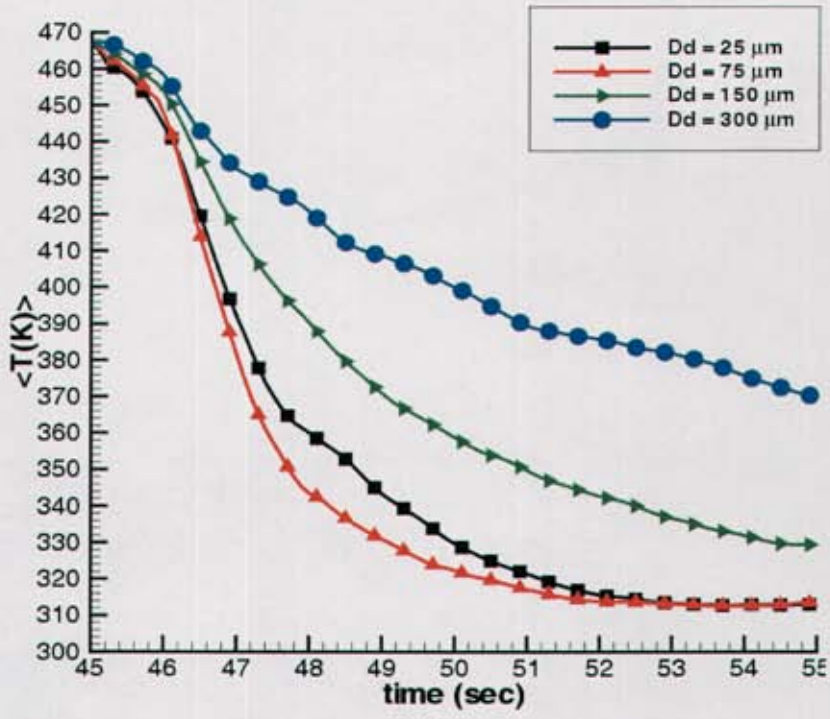

(b)

Figure 4-9 Volume averaged temperature for configuration 2 showing (a) <Tl> and (b) <Tu> verses time.

CHAPTER 5 SUMMARY

5.1 Overview and Conclusions

A two-phase spray dilute model is developed for application to fire phenomena. The model is based on phase-averaging principles resulting in transport equations for the liquid and gas phases. Analysis of the phase-averaging procedure identified several issues related to the application of volume averaging to multiphase flows

- The use of non-uniform filters is desirable from a CFD implementation standpoint. However, the introduction of non-uniform filters introduces two difficult to treat issues. The first is commutation error and the second is the surface integral term that is expressed in terms of transformed computational space for which constitutive properties are not easily obtained.
- For these reasons, a uniform filtering approach is pursued to develop the phase-averaged transport equations.

Phase averaging the transport equations results in a set of equations for the gas and liquid phases. The gas phase system is solved using existing algorithms in VULCAN and supplemented with source terms representing the effects of the liquid droplets. The liquid phase is treated using a Lagrangian stochastic separated flow approach with submodels to account for droplet transport, evaporation, dispersion due to turbulence, breakup and collision as well as several injection methods are developed and implemented.

A V&V strategy plan is presented for testing and evaluation of the spray model. The problems in this plan are chosen to progressively add more complexity to the subgrid models as confidence is gained in the predictive capability. Results are presented for a subset of these problems ranging from simple particle dispersion in turbulent flows, to water spray suppression of enclosure fires. Specifically the following conclusions are drawn from the cases examined.

- The simple random walk turbulence model performs well for heavier particles that are representative of drops that would exist for spray modeling that is applicable to fire simulation. In the limit of fluid particle dispersion, the random walk model matches well with published analytical solutions and experimental data for grid generated turbulence and turbulent free round jets.
- The major findings from water spray suppression of enclosure fires are: 1) application of water spray with large drops may actually increase the local temperature before cooling can take place due to accelerated burning from enhanced turbulent mixing and 2) an optimum drop size for suppression was observed which allows for maximum decrease in gas-phase temperature for a given water mass loading.

5.2 Recommendation for Future Work

The primary need for future work is further V&V of the current spray model for the problems listed in Table 4-1. In addition, the spray model development discussed in this report is certainly not comprehensive and the model would benefit from additional research. Some of the more important areas with regard to fire phenomena are summarized in the following subsections.

5.2.1 Radiation Transport

The effects of thermal radiative heat exchange among the drops and to the surrounding is currently neglected. Accounting for these effects may have an effect on the results for spray suppression where high levels of thermal radiation from fires will tend to enhance vaporization of droplets before they reach a flame zone. Recently, Consalvi *et al.* [105] applied a formal phase-averaging procedure to the radiative transfer equation in particulate media. In their approach, the gas phase absorptivity and scattering is assumed constant over the phase-averaging volume and the particulate phase is treated as a collection of large diffusely reflecting spheres. This approach could be extended for use with water sprays by including scattering phase functions for water droplets and introducing anisotropic scattering into the discrete transfer method currently employed in VULCAN. Alternatively, gridless approaches, such as developed by Gritzo *et al.* [106], could also be pursued to account for radiation exchange between clouds of droplets. In this approach the integral form of the radiative transfer equation for emitting and absorbing media is used with algorithms based on multipole fast solvers and a binary tree domain decomposition for execution on massively parallel computing architectures. Similar to the grid based schemes, the gridless radiation algorithm would have to be extended to include the effects of scattering media for application to sprays.

5.2.2 Droplet Impact Model

Due to its wide range of applicability, several studies have been conducted on droplet impact and discussed in the excellent reviews on the subject by Healy *et al.* [60] and Rein [61]. Previous work on droplet impact has largely focused on the spreading rate and maximum splat size of individual droplets as a function of surface temperature, roughness, wetting conditions and initial droplet Weber number. These studies include detailed high-speed photography measurements and numerical simulations of water [62-70], heptane [71,72], molten metals [73,74] and, more recently, liquid fire suppressants [75,76]. However, to the authors' knowledge, there has not been a simplified phenomenological model for droplet impact that is suitable for numerical simulation of sprays involving thousands of droplets.

The impact of droplets with solid surfaces involves the large deformation of the droplet into a flat disc shape, and at high enough momentum, possible secondary atomization due to droplet shattering. These events all occur at time and length scales that cannot be possibly resolved from first principals for a large spray simulation. A phenomenological based model description for droplet impact is therefore required. The model would have to be capable to account for the distinct physical processes of droplet adhesion, breakup and shattering, and bouncing, as illustrated in Fig. 5-2. These events will depend in general on many factors including the thermal properties of the agent (viscosity and surface tension), droplet momentum, angle of impact, surface temperature and surface roughness.

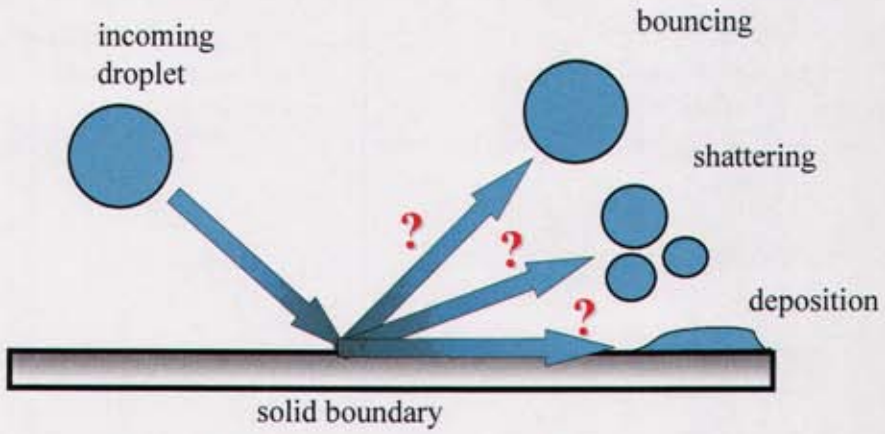

Figure 5-1 Illustration of possible droplet impact events.

Preliminary work in this area can be found in the Ref. [77]. The impact model in this study is formulated using mass and energy conservation principles along with established correlations for breakup of individual droplets. Results using this model show the model is able to capture the distinct droplet impact regimes ranging from droplet bouncing to deposition to shattering.

5.2.3 Droplet Group Vaporization and Combustion

Most of the modeling approaches for two-phase sprays are based on single droplet evaporation. As in this work, a spray is then assumed to be simply a linear superposition of a large number of single drops. The influence of droplet-droplet drag wake effects on drag and evaporative processes are usually not taken into account. For combusting sprays the effects of group combustion burning models have been investigated by Chiu *et al* [12,78-80], Akamatsu *et al.* [81], Correa and Sichel [83], Labowsky and Rosner [82] and Kerstein and Law [84]. Simply described, the basic idea behind these approaches is not to treat a spray as a collection of burning drops but rather as a cloud surrounded by a flame as illustrated in Fig. 5-2.

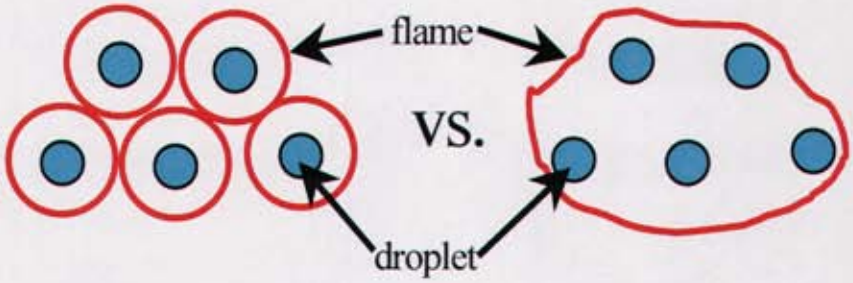

Figure 5-2 Illustration of group burning mode.

The focus of this effort would be to adapt some of the concepts associated with group modeling to the current SSF formalism.

5.2.4 Turbulence Modulation due to Droplet Transport

Previous studies have shown that the presence of drops or particles in a flow may signifi-

cantly modulate the turbulent intensity [85-89]. Based on a compilation of many experiments on particle laden flows, Crowe *et al.* [85-87] observed that the change in turbulent kinetic energy is strongly dependent on the ratio of the particle size to the integral length scale, D_d/L_T. For flow regimes where $D_d/L_T < 1$, the effect of the particle results in a decrease of the turbulence intensity while an increase in turbulence intensity is observed for $D_d/L_T > 1$. The physical reasoning provided for this observation is that often small droplets move with the turbulent eddies therefore draining energy from the larger eddies to carry the droplets. However, if the droplets are larger than they are less response to the fluid motion and actually create turbulent kinetic energy from the generation of wakes.

The direct modulation of the turbulence due to droplets is not currently taken into account in the spray model, but only indirectly through the generation of shear from changes in gas-phase momentum. The effects of turbulence modulation can be readily incorporated into the future revisions of the model by introducing source terms into the k and ε transport equations which are functions of the local droplet field [87].

REFERENCES

[1] Jones, W. P. and Launder, B.E., "The Prediction of Laminarization with a Two-equation Model of Turbulence," *Int J. of Heat Mass Transfer*, vol. 15, pp. 301-314, 1972.

[2] Byggstøyl, S. and Magnussen, B.F., "Finite Difference Calculation of Pool Fires," In *Proceedings of the twenty-third Symp. (Int.) on Combustion*, pp. 1677-1683, The Combustion Institute, Pittsburgh, PA, 1990.

[3] Magnussen, B.F., Particle Carbon Formation During Combustion, Plenum Publishing Corp., 1981.

[4] Lockwood, F.C. and Shah, N.G., "A New Radiation Solution Method for Incorporation in General Combustion Prediction Procedures," In *Proceedings of the eighteenth Symp. (Int.) on Combustion,* pp. 1405-1414, The Combustion Institute, Pittsburgh, PA, 1981.

[5] Patankar, S.V., Numerical Heat Transfer and Fluid Flow, Hemisphere Publishing Co, New York, NY, 1980.

[6] Tieszen, S. R., Nicolette, V. F., Gritzo, L. A., Holen, J. K., Murray, D. Moya, J.L., "Vortical Structures in Pool Fires: Observation, Speculation, and Simulation," Sandia National Laboratory Report, SAND96-2607, 1996.

[7] Black, A. R., Gill, W., Suo-Anttila, J. M., Tiesen, S. R., Gritzo, L. A., "Numerical Predications and Experimental Results of a Dry Bay Fire Environment," Sandia National Laborartory Report, in progress, 2002.

[8] Tieszen, S. R., Black, A. R., Moen, C. D., Chu, T. Y., Nicolette, V. F., Gill, W. Burns, S. P., Moffatt, W. C., 2001, "SIERRA/FUEGO and SIERRA/SYRINX Verification and Validation Plan Version 2.0," Sandia National Laboratories, Albuquerque, NM, SAND2001-3798, 2001.

[9] Faeth, G. M., "Evaporation and Combustion of Spray," *Prog. Energy Combust. Sci.*, vol. 9, pp. 1-76, 1983.

[10] Crowe, C. and Sommerfeld, M. and Tsuji, Y., Multiphase Flows with Droplets and Particles, CRC Press, New York, NY, 1998.

[11] Loth, E., "Numerical Approaches for Motion of Dispersed Particles, Droplets, and Bubbles," *Prog. in Energy and Combust. Sci.*, Vol. 26, pp. 161-223, 2000.

[12] Chiu, H.H., "Advances and Challenges in Droplet and Spray Combustion. I. Towards a Unified Theory of Droplet Aerothermochemistry," *Progress in Energy and Combustion Science*, vol. 26, pp. 381-416, 2000.

[13] Faeth, G. M., "Mixing, Transport and Combustion in Sprays," *Prog. Energy Combust. Sci.*, pp. 293-345, vol. 13, 1987.

[14] Maxey, M. R. and Riley, J. J., "Equation of Motion for a Small Rigid Sphere in a Nonuniform Flow," *Phys. Fluids*, vol. 26, no. 4, pp. 883-889, 1983.

[15] Chhabra, R.P, Agarwal, L. and Sinha, N.K., "Drag on Non-spherical Particles: An Evaluation of Available Methods," *Powder Technology*, vol. 101, pp. 288-295, 1999.

[16] Kuo, K. K., Principles of Combustion, A Wiley-Interscience Publication, John

Wiley & Sons, New York, NY, 1986.

[17] Watson, K. M., "Predication of Critical Temperature and Heats of Vaporization," *Ind. Eng. Chem.*, pp. 360-364, vol. 23, 1931.

[18] Lefebvre, A. H., Atomization and Sprays, Hemisphere Publishing Corporation, New York, NY, 1989.

[19] Sirignano, W. A., Fluid Dynamics and Transport of Droplets and Sprays, Cambridge University Press, 1999.

[20] Gosman, A. D. and Ioannides, E., "Aspects of Computer Simulation of Liquid-Fueled Combustion," AIAA paper, 81-0323, 1981.

[21] Shuen, J-S. and Chen, L-D. and Faeth, G.M., "Evaluation of a Stochastic Model of Particle Dispersion in a Turbulent Round Jet," *AIChE Journal*, vol. 29, pp. 167-170, 1983.

[22] Zhou, Q. and Yao, S.C., "Group Modeling of Impacting Spray Dynamics," *Int. J. Heat Mass Transfer*, vol. 35, no. 1, pp. 121-129, 1992.

[23] Hinze, J. O., Turbulence, McGraw Hill Book Company, New York, NY, 1975.

[24] Ranz, W. E. and Marshall, W.R., "Evaporation from Drops," *Chem. Engrg. Prog.*, vol. 48, pp. 141-173, 1952.

[25] Amsden, A.A., Ramshaw, J.D., O'Rourke, P. and Dukowicz, J.K., "KIVA: A Computer Program for Two-and Three-Dimensional Fluid Flows with Chemical Reactions and Fuel Sprays," Los Alamos Report, LA-10245, 1985.

[26] Reitz, R. D., "Modeling Atomization Processes in High-Pressure Vaporizing Sprays," *Atomisation and Spray Technology*", vol. 3, pp. 309-337, 1987.

[27] Liu, A.B., Mather, D. and Reitz, R.D., "Modeling the Effects of Drop Drag and Breakup on Fuel Sprays," SAE Technical Paper 930072, 1993.

[28] O'Rourke, P.J. and Amsden, A.A., "The Tab Method for Numerical Calculation of Spray Droplet Breakup," SAE Technical Paper, 872089, 1987.

[29] Ashgriz, N. and Givi, P., "Coalescence Efficiencies of Fuel Droplets in Binary Collisions,", *Int. Comm. Heat Mass Transfer,* vol. 16, pp. 11-20, 1989

[30] Qian, J. and Law, C.K., "Regimes of Coalescence and Separation in Droplet Collision," *J. Fluid Mech.*, vol. 331, pp. 59-80.

[31] Estrade, J.-P. , Carentz, Hervé, "Experimental Investigation of Dynamimc Binary Collision of Ethanol Droplets - A Model from Droplet Coalescence and Bouncing," *Int. J. of Heat and Fluid Flow*, vol. 20, pp. 486-491, 1999.

[32] Ibrahim, E.A., Yang, H.Q. and Przekwas, A.J., "Modeling of Spray Droplets Deformation and Breakup," *J. Propulsion*, vol. 9, no. 4, pp. 651-654, 1993.

[33] Gorokhavski, M., "Stochastic Spectral Relaxation Model of Drops Break-Up in Liquid Spray Compuations," AIAA paper 2000-0193, 38th Aerospace Sciences Meeting & Exhibt, Reno, NV, 2000.

[34] Gorokhovski, M. and Apte, S., "Stochastic Sub-grid Modeling Drop Breakup for LES of Atomizing Spray," Center for Turbulence Research Annual Research Briefs, pp. 169-176, 2001.

[35] O'Rourke, P., "Collective Drop Effects on Vaporizing Liquid Sprays," Los Alamos National Laboratory Report No. LA-9069-T, 1981.

[36] Georjon, T.L. and Reitz, R.D., "A Drop-Shattering Collision Model for Multidimensional Spray Computations," *Atomization and Sprays*, vol. 9, pp. 231-254, 1999.

[37] Brazier-Smith, P.R., Jennings, S.G. and Latham, J., "The Interaction of Falling Water Drops: Coalescence," *Proc. R. Soc. Lond. A.*, vol. 326, pp. 393-408, 1972.

[38] Radhakrishnan, K. and Hindmarsh, A.C., "Description and use of LOSDE, the Livermore Solver for Ordinary Differential Equations," Technical Report UCRL-ID-113855, Lawrence Livermore National Laboratory, Livermore, CA, 1993.

[39] Chapra, S.C. and Canale, R.P., Numerical Methods for Engineers, second edition, McGraw-Hill Book Company, New York, NY, 1988.

[40] Amsden, A. A. and Ramshaw, J.D. and Cloutman, L. D. and O'Rourke, P. J., "Improvements and Extensions to the KIVA Computer Program," LA-10534-MS, Los Alamos, NM, 1985.

[41] Snyder and Lumely, "Some Measurements of Particle Velocity Autocorrelation Functions in Turbulent Flow," *J. Fluid Mech.*, vol. 48, pp. 41-71, 1971.

[42] Wells, M.R., and Stock, D.E., "The Effects of Crossing Trajectories on the Dispersion of Particle in a Turbulent Flow," *J. Fluid Mech.*, vol. 136, pp. 31-62, 1983.

[43] Chen, J.-H. and Faeth, G.M., "Measurements and Predictions of Turbulence Generation in Homogeneous Particle-Laden Flows", AIAA paper, AIAA 2000-0182, 2000.

[44] MacInnes, J. M. and Bracco, F. V., "Stochastic Particle Dispersion Modeling and the Tracer-particle Limit," vol. 4, pp. 2809-2824, *Phys. Fluids A*, 1992.

[45] Berlemont, A., Desjonqueres, P. and Gouesbet, G., "Particle Lagrangian Simulations in Turbulent Flows," *Int. J. Muliphase Flow*, Vol. 16, pp. 19-34, 1990.

[46] Shirolkar, J. S. and McQuay, M. Q., "Probability Density Function Propagation Model for Turbulent Particle Dispersion," *Int. J. Muliphase Flow*, Vol. 24, pp. 663-678, 1998.

[47] Lu, Q. Q., Fontaine, J.R. and Aubertin, G., "Numerical Study of the Solid Particle Motion in Grid-generated Turbulent Flows," *Int. J. Heat Mass Transfer*, Vol. 36, pp. 79-87, 1993.

[48] Yuu, S., Yasukouchi, N., Hirosawa, Y. and Jotaki, T., "Particle Turbulent Diffusion in a Dust Laden Round Jet," *AIChE Journal*, vol. 24, pp. 509-519, 1978.

[49] Shuen, J-S. and Chen, L-D. and Faeth, G.M., "Evaluation of a Stochastic Model of Particle Dispersion in a Turbulent Round Jet," *AIChE Journal*, vol. 29, pp. 167-170, 1983.

[50] McDonell, V.G. and Samuelsen, G.S., "Structure of Vaporizing Pressure Atomized Sprays," *Atomization and Sprays*, pp. 321-364, vol. 3, 1993

[51] McDonell, V.G., Adachi, M. Samuelsen, G.S., "Structure of Reacting and Nonreacting, Nonswirling, Air-Assisted Sprays, Part I: Gas-Phase Properties," *Atomization and Sprays*, pp. 389-410, vol. 3, 1993

[52] McDonell, V.G., Adachi, M. and Samuelsen, G.S., "Stucture of Reacting and Non-reacting, Nonswirling, Air-Assisted Sprays, Part II: Drop Behavior," *Atomization and Sprays*, pp. 411-436, vol. 3, 1993

[53] Widmann, J. F., Charagundla, S.R., Presser, C. and Heckert, A., "Benchmark Experimental Database for Multiphase Combustion Model Input and Validation: Baseline Case," National Institute of Standards and Technology Report, NISTIR 6286, 1999.

[54] Chiang, C.H., Raju, M.S. and Sirignano, W.A., "Numerical Analysis of Convecting, Vaporizing Fuel Droplet with Variable Properties," *Int. J. Heat Mass Transfer*, vol. 35, pp. 1307-1324, 1992.

[55] Skaggs, R., "Experimental Characterization of Water and Diesel Fuel Sprays," Army Research Laboratory Technical Report, ARL-TR-2599, 2001.

[56] Ayers, S., Anleitner, B., Maranghides, A., Borman, B. and Sheinson. R, "Preliminary Fire Suppression Experiments with Water Spray in a 28 m3 (1000 ft3) Compartment," NRL Report 6180/0446A:RSS (in progress), 2002.

[57] Drysdale, D., An Introduction to Fire Dynamics, Second Edition, John Wiley & Sons, New York, NY, 1998.

[58] Atreya, A., Crompton, T. and Suh, J., "An Experimental and Theoretical Study of Mechanisms of Fire Suppression by Water." NIST Report NISTIR 5499, 1994.

[59] Grant, G., Brenton J. and Drysdale, D., "Fire Suppression by Water Sprays," *Prog. Energy Combust. Sci.*, 26, 79-130, 2000.

[60] Healy, W. M., Hartely, J.G. and Abdel-Khalik, S.I., "Comparison Between Theoretical Models and Experimental Data for the Spreading of Liquid Droplets Impacting a Solid Surface," *Int. J. Heat Mass Transfer*, 39, pp. 3079-3082, 1996.

[61] Rein, M., "Phenomena of Liquid Drop Impact on Solid and Liquid Surfaces," *Fluid Dynamics Research*, 12, pp. 61-93, 1993.

[62] Foote, G.B., "The Water Drop Rebound Problem: Dynamics of Collision," *Journal of the Atomosphereic Sciences*, vol. 32, 1974.

[63] Tsurutani, K., Yao, M., Senda, J. and Fujimoto, H., "Numerical Analysis of the Deformation Process of a Droplet Impinging upon a Wall," *JSME Int. Journal*, vol. 33, pp. 555-561, 1990.

[64] Fukai, J., Zhao, Z., Poulikakos, D., Megaridis, C.M. and Miyatake, O., "Modeling of the Deformation of a Liquid Droplet Impinging Upon a Flat Surface," *Phys. Fluids*, vol. 5, pp. 2588-2599, 1993.

[65] Fukai, J. Shiiba, Y., Yamamoto, T., Miyatake, O., Poulikakos, D., Megaridis, C.M. and Zho, Z., "Wetting Effects on the Spreading of a Liquid Droplet Colliding with a Flat Surface: Experiment and Modeling," *Phys. Fluids*, vol. 7, pp. 236-247, 1995.

[66] Pasandideh-Fard, M., Qiao, Y.M., Chandra, S. and Mostaghimi, J., "Capillary Effects During Droplet Impact on a Solid Surface," *Phys. Fluids*, vol. 8, pp. 650-659, 1996.

[67] Bernardin, J.D., Stebbins, C.J. and Mudawar, I., "Effects of Surface Roughness on Water Droplet Impact History and Heat Transfer Regimes," *Int. J Heat and Mass Transfer*, vol. 40, pp. 73-88, 1997.

[68] Hung, L.S. and Yao, S.C., "Experimental Investigation of the Impaction of Water Droplets on Cylindrical Objects," *Int. J. of Multiphase Flow*, vol. 25, pp. 1545-1559, 1999.

[69] Bussmann, M., Mostaghimi, J. and Chandra, S., "On a Three-Dimensional Volume Tracking Model of Droplet Impact," *Phys. Fluids*, vol. 11, pp. 1406-1417, 1999.

[70] Hung, L.S. and Yao, S.C., "Experimental Investigation of the Impaction of Water Droplets on Cylindrical Objects," *Int. J. of Muliphase Flow,* vol. 25, pp. 1545-1559, 1999.

[71] Chandra, S. and Avedisian, C.T., "On the Collision of a Droplet with a Solid Surface," *Proc. R. Soc. Lond. A*, vol. 432, pp. 13-41, 1991.

[72] Harvie, D.J.E. and Fletcher, D.F.,"A Hydrodynamic and Thermodynamic Simulation of Droplet Impacts on Hot Surfaces, Part II: Validation and Application," *Int. J. of Heat and Mass Transfer*, vol. 44, pp. 2643-2659, 2001.

[73] Pasanddideh-Fard, M., Bhola, R., Chandra, S. and Mostaghimi, J., "Deposition of Tin Droplets on a Steel Plate: Simulations and Experiments," *Int. J. of Heat and Mass Transfer*, vol. 41, pp. 2929-2945, 1998.

[74] Aziz, S. D. and Chandra, S., "Impact, Recoil and Splashing of Molten Metal Droplets," *Int. J. of Heat and Mass Transfer*, vol. 43, pp. 2841-2857, 2000.

[75] Manzello, S. L. and Yang, J.C., "An Experimental Study of High Weber Number Impact of Methoxynonaflourobutance C4F9OCH3 (HFE-7100) and N-heptane Droplets on a Heated Solid Surface," *Int. J. of Heat and Mass Trans.*, accepted for publication, 2002.

[76] Manzello, S. L. and Yang, J.C., "On the Collision Dynamics of a Water Droplet Containing an Additive on a Heated Solid Surface," *Proc. Roy. Soc. London A.*, accepted for publication, 2002.

[77] DesJardin, P.E., Presser, C., Disimile, P.J. and Tucker, J.R., "A Droplet Impact Model for Agent Transport in Engine Nacelles," *Proceedings of the Halon Options Technical Working Conference*, 2002.

[78] Chiu, H.H. and Liu, T.M., "Group Combustion of Liquid Droplets," *Combust. Sci. Technol.*, vol. 17, pp. 127-131, 1977.

[79] Chiu, H.H., Kim, H.Y. and Croke, E.J., "Internal Group Combustion of Liquid Droplets," In the *Proceedings of the Nineteenth Symposium (Int.) on Combustion,* pp. 971-980, The Combustion Institute, Pittsburgh, PA, 1982.

[80] Chiu, H.H. and Lin, C.L., "Anomalous Group Combustion of Premixed Clusters," In the *Proceedings of the Twenty-sixth Symposium (Int.) on Combustion*, pp. 1653-1661, The Combustion Institute, Pittsburgh, PA, 1996.

[81] Akamatsu, F., Mizutani, Y., Katsuki, M., Tsushima, S. and Cho, Y.D., "Measurements of the Local Group Combustion Number of Droplet Clusters in a Premixed Spray Stream," In the *Proceedings of the Twenty-sixth Symposium (Int.) on Combustion*, pp. 1723-1729, The Combustion Institute, Pittsburgh, PA, 1996.

[82] Labowsky, M. and Rosner, D.C., "Group Combustion of Droplets in Fuel Clouds I. Quasi-Steady Predictions," in *Evaporation-Combustion of Fuels*, vol. 166 of

Advances in Chemistry Series, J.T. Zung, ed., pp. 63-79, Americal Chemical Society, Washington, D.V., 1978.

[83] Correa, S.M. and Sichel, M., "The Group Combustion of a Spherically Cloud of Monodisperse Fuel Droplets," in the *Proceedings of the Nineteenth Symposium (Int.) on Combustion*, pp. 981-991, The Combustion Institute, Pittsburgh, PA., 1983.

[84] Kerstein, A.R. and Law C.K., "Percolation in Combustion Sprays. I. Transition from Cluster Combustion to Percolate Combustion in Non-Premixed Sprays," in the *Proceedings of the Ninetheeth Symposium (Int.) on Combustion*, pp. 961-970, The Combustion Institute, Pittsburg, PA, 1983.

[85] Gore, R.A. and Crowe, C.T., "Effect of Particle Size on Modulating Turbulent Inensity," *Int. J. Multiphase Flow*, vol. 15, pp. 279-285, 1989.

[86] Crowe, C.T., "Modeling Turbulence in Multphase Flows," In *Engineering Turbulence Modelling and Experiments 2*, Editors W. Rodi and F. Martelli, Elsevier Sciences Publishers B.V., pp. 899-913, 1993

[87] Crowe, C. T., "On Models for Turbulence Modulation in Fluid-particle Flows," *International Journal of Muliphase Flow*, vol. 26, pp. 719-727, 2000.

[88] Boivin, M., Simonin, O. and Squires, K.D., "Direct Numerical Simulation of Turbulence Modulation by Particles in Isotropic Turbulence," *J. Fluid Mech.*, vol. 375, pp. 235-263, 1998.

[89] Li, C., Mosyak, A. and Hetsroni, G., "Direct Numerical Simulation of Particle-Turbulence Interation," *Int. J. of Multiphase Flow*, vol. 25, pp. 187-200, 1999.

[90] Travis, J.R., Harlow, F.H. and Amsden, A.A., "Numerical Calculation of Two-Phase Flows," *Nuclear Science and Engineering*, vol. 61, pp. 1-10, 1976.

[91] Anderson, T. B. and Jackson, R., "A Fluid Mechanical Description of Fluidized Beds," *I&EC Fundamentals*, vol. 6, no. 4, 1967.

[92] Gray, W. G. and Lee, P. C. Y., "On the Theorems for Local Volume Averaging of Multiphase Systems," *Int. J. Multiphase Flow*, vol. 3, pp. 333-340, 1977.

[93] Gough, P. S. and Zwarts, F. J., "Modeling Heterogeneous Two-Phase Reacting Flow," *AIAA Journal*, vol. 17, no. 1, pp. 17-25,1979.

[94] Slattery, J.C., "Flow of Viscoelastic Fluids Through Porous Media," *A.I.Ch.E. J.*, vol. 13, pp. 1066- , 1967.

[95] Slattery, J. C., Momentum Energy and Mass Transfer in Continua, second edition, Robert E. Krieger Publishing Company, Inc., 1981.

[96] Whitkar, S., "Advances in the Theory of Porous Media," *Ind. Engng. Chem.*, vol. 61, pp. 14-28, 1969.

[97] Whitkar, S., "The Transport Equations for Multi-phase Systems," *Chemical Engineering Science*, vol. 28, pp. 139-147, 1973.

[98] Oefelein, J. C. and Yang, V., "Simulation of High-Pressure Spray Field Dynamics," in *Recent Advances in Spray Combustion: Spray Atomization and Drop Burning Phenomena* in Progress in Astronautics and Aeronautics, vol. 2, 1996.

[99] Zhu, M., Bray, K.N., Rumberg, O. and Rogg, B., "PDF Transport Equations for Two-Phase Reactive Flows and Spray," *Combustion and Flame*, vol. 122, pg. 327-

338, 2000.

[100] Archambault, M. R. and Edwards, C.F., "Computation of Spray Dynamics By Direct Solution of Moment Transport Equations," AIAA 2000-0197, *38th Aerospace Sciences Meeting & Exhibit*, Reno, NV, 2000.

[101] Ghosal, S. and Moin, P., "Basic Equations for the Large Eddy Simulation of Turbulent Flow in Complex Geometry," *J. Comput. Phys.*, vol. 118, no. 1, pp. 24-37, 1995.

[102] Hildebrand, F. B., Advanced Calculus for Applications, pp.348-350, Prentice-Hall, Inc., Englewoods Cliffs, NJ, 1962.

[103] Vasilyev, O.V., Lund, T.S. and Moin, P., "A General Class of Commutative Filters for LES in Complex Geometries," *J. Comput. Phys.*, vol. 146, no. 1, pp. 82-104, 1998.

[104] van der Ven, H., "A Family of Large Eddy Simulation (LES) Filters with Nonuniform Filter Widths," *Phys. Fluids*, vol. 7, no. 5, pp. 1171-1172, 1995.

[105] Consalvi, J.L, Porterie, B. and Loraud, J.C., "A Formal Averaging Procedure for Radiation Heat Transfer in Particulate Media," *Int. J. of Heat and Mass Trans.*, vol. 45, pp. 2755-2768, 2002.

[106] Gritzo, L.A., Strickland, J.H. and DesJardin, P.E., "Radiation in an Emitting and Absorbing Medium: A Gridless Approach," Sandia National Laboratory Report, SAND2000-0960, 2000.

[107] Pedras, M.H.J. and deLemos, M.J.S., "Macroscopic Turbulence Modeling for Incompressible Flow Through Undeformable Porous Media," *Int. J. of Heat and Mass Transfer*, vol. 44, pp. 1081-1093, 2001.

[108] Pedras, M. H. J. and de Lemos, M. J. S., "On the Definition of Turbulent Kinetic Energy for Flow in Porous Media," *Comm. Heat Mass Transfer*, 27, pp.211-220, 2000.

[109] Antohe, B.V. and Lage, J.L., "A General Two-equation Macroscopic Turbulence Model for Incompressible Flow in Porous Media," *Int. J. Heat and Mass Transfer*, vol 40, pp. 3013-3024, 1997.

[110] Nakayama, A. and Kuwahara, F., "A Macroscopic Turbulence Model for Flow in a Porous Medium," *ASME Journal of Fluids Engineering*, vol. 121, 1999.

[111] Aldama, A.A., "Filtering Techniques for Turbulent Flow Simulations," Lecture Notes in Engineering, vol. 49, Springer-Verlag, New York, NY, 1990.

APPENDIX A MATHEMATICAL THEORY OF TWO-PHASE AVERAGING

The phase averaged transport equations are derived to identify the source terms that are needed in the gas-phase transport equations to account for the effects of the spray. Phase-averaged transport equations can be obtained by either taking moments of the spray equation PDF transport equation [90] or alternatively by volume averaging the conservation equations directly. In this appendix, the latter approach will be discussed in detail.

The following is a brief review of the mathematics of two-phase averaging for the benefit of the reader who is not readily familiar the background of volume averaging. In addition, new concepts related to commutation error presented in the LES literature [1,2] are adapted for application to two-phase averaging to show the errors introduced when the spatial averaging volume is allowed to change as a function of position.

The formal averaging for two-phase media was first introduced by Anderson and Jackson [91] through the use of a local filtering function and later refined by Gray *et al.* [92] and Gough *et al.* [93] as presented in text book form by Kuo [16]. Alternatively, Slattery [94,95] and Crowe [10] offer a different derivation based on a spatially dependent volume of integration. The presentation here follows the outline of Kuo is somewhat different than have been developed in classical two-phase flow literature [96,97] and incorporates spatial filtering issues found in the LES literature such as commutation error. Figure A-1 illustrates a typical phase averaging volume showing the total volume of interest, V_T, the total volume of all of the drops, V_l, and the volume of the gas, V_g.

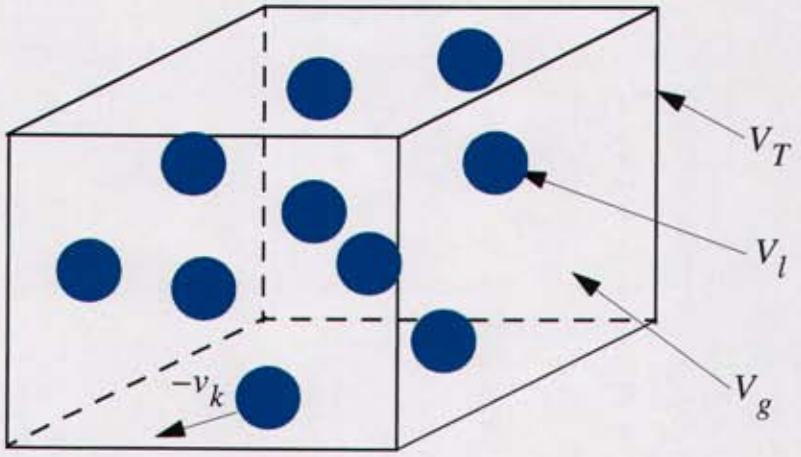

Figure A -1 Illustration of phase averaging volume with droplets.

Phase averaged properties are obtained by first defining a spatial filtering function, $G((x_i - x'_i)/\Delta_f)$, with the normalization property: $\int_{V_\infty} G((x_i - x'_i)/\Delta_f)dV' = 1$.

For volume averaging using a cubic volume of length $l_T = (V_T)^{1/3}$ on a side then $\Delta_f = l_T$ and G is defined as $G = \frac{1}{V_T}\prod_{i=1}^{3}[H(x'_i - x_i + \Delta_f/2) - H(x'_i - x_i - \Delta_f/2)]$ where H is the Heaviside function. Convoluting G with the a property of interest, β, yields the average gas phase quantity,

$$\langle\beta(x_i)\rangle = \int_{V_{g_\infty}} \beta(x'_i) G\left(\frac{x_i - x'_i}{\Delta_f}\right) dV' \qquad \text{(A-1)}$$

and physically represents a spatially averaged property over the volume V_T. It should be emphasized that the volume of integration, V_{g_∞}, represents all of regions occupied by the gas and so does not depend on the location, x_i, where the averaging takes place. Of more value is the intrinsic average, $\hat{\beta}$, defined as the local average of β over the gas phase volume, V_g, for which constitutive and thermodynamic properties exist. The intrinsic average is defined as: $\hat{\beta} = \langle\beta\rangle/\phi$ and is the variable of interest to solve for after phase averaging the transport equations for mass, momentum, species and energy (to be discussed in section A.2). The variable ϕ is the void fraction and is defined as the volume of the gas divided by the entire averaging volume, *i.e.*, $\phi = V_g/V_T$.

A.1 Temporal and Spatial Derivatives for Phase Averaging

Applying the spatial filtering function to the transport equations requires expressing the phase averaged time and spatial partial derivatives in terms of temporal and spatial derivatives of phase averaged quantities. The volume of the gas phase is assumed to change as a function of both time and space due to droplet evaporation.

A.1.1 Time derivatives

Relations for the temporal derivative are obtained by taking the partial derivative of $\langle\beta\rangle$.

$$\frac{\partial}{\partial t}\langle\beta\rangle = \frac{\partial}{\partial t}\int_{V_{g_\infty}(t)} \beta(x_i') G\left(\frac{x_i - x_i'}{\Delta_f}\right) dV' \qquad \text{(A-2)}$$

Since the volume of the gas is a function of time, Leibnitz rule [12] has to be applied to commute the temporal derivative term inside the volume averaging operator as follows:

$$\frac{\partial}{\partial t}\langle\beta\rangle = \int_{V_{g_\infty}(t)} G\left(\frac{x_i - x_i'}{\Delta_f}\right)\frac{\partial}{\partial t}(\beta(x_i'))dV' + \int_{A_{g_\infty}(t)} G\left(\frac{x_i - x_i'}{\Delta_f}\right)\beta(x_i')v_k(x_i')dA'_k. \qquad \text{(A-3)}$$

In Eq. (A-3), the first term on the right hand size is the definition of the phase averaged time rate in change of β, *i.e.*, $\langle\partial\beta/\partial t\rangle$. The second term is a surface integral that accounts for

material crossing the boundary of the phase averaging volume as a function of time, where v_k is the velocity of the phase averaging surface (A_g with direction pointing into the droplet). The gas phase surface is further broken into the contribution associated with the droplets, A_l, and rest of the surface area associated with the phase averaging volume, A_{g-l}. Since G goes to zero at the boundary on the surface A_{g-l} then that contribution of the surface integral can be ignored leading to the following relation for the phase averaged time derivative that will become useful when deriving the phase averaged transport equations in section A.2.

$$\langle\frac{\partial\beta}{\partial t}\rangle = \frac{\partial}{\partial t}\langle\beta\rangle - \int_{A_d} G\left(\frac{x_i - x_i'}{\Delta_f}\right)\beta(x_i')v_k(x_i')dA'_k \qquad \text{(A-4)}$$

A.1.2 Space derivatives with uniform filter width

Analogous to the time derivatives, a spatial derivative relation is obtained by taking the divergence of a phase averaged vector quantity.

$$\frac{\partial}{\partial x_j}\langle\beta_j(x_i)\rangle = \frac{\partial}{\partial x_j}\int_{V_{g_\infty}} \beta_j(x_i')G\left(\frac{x_i - x_i'}{\Delta_f}\right)dV' \qquad \text{(A-5)}$$

Since the volume averaging is independent of the location then the partial derivative can be brought inside the integration and applied directly to the filtering function G.

$$\frac{\partial}{\partial x_j}\langle\beta_j(x_i)\rangle = \int_{V_{g_\infty}} \beta_j(x_i')\frac{\partial}{\partial x_j}G\left(\frac{x_i - x_i'}{\Delta_f}\right)dV' \qquad \text{(A-6)}$$

For uniform filter size (*i.e.*, $\Delta_f = const$) and $\partial G/\partial x_j = -\partial G/\partial x'_j$ (chain rule of differentiation) and Eq. (6) can be expressed as:

$$\frac{\partial}{\partial x_j}\langle\beta_j(x_i)\rangle = \int_{V_{g_\infty}} \left(G\left(\frac{x_i - x_i'}{\Delta_f}\right)\frac{\partial}{\partial x_j'}\beta_j(x_i') - \frac{\partial}{\partial x_j'}\left[\beta_j(x_i')G\left(\frac{x_i - x_i'}{\Delta_f}\right)\right]\right)dV'. \qquad \text{(A-7)}$$

The first term on the right hand size of Eq. (A-7) is the phase averaged β_j gradient. The second term can be further expressed in terms of a surface integral using the divergence theorem. Rearranging terms leads to an expression for the phase averaged divergence of β_j in terms of the divergence of $\langle\beta_j\rangle$ and a surface integral exchange term (SET) that accounts for the presence of droplets.

$$\langle\frac{\partial}{\partial x_j}\beta_j(x_i)\rangle = \frac{\partial}{\partial x_j}\langle\beta_j(x_i)\rangle + \underbrace{\int_{A_l}\beta_j(x_i')dA'_j dA}_{\text{SET}} \qquad \text{(A-8)}$$

An important assumption in the derivation of Eq. (A-8) is the filter width is assumed to be *constant*. That is, the filter width is assumed to be invariant with space and time. In practice it would be convenient to relate the filter width to a multiple size of the CFD grid in order to

readily determine the number of cells that constitute the local filtering region of interest. Since the CFD cells change size then the filter width size would change as well. Therefore, the use of a non-uniform filtering volume is investigated.

A.1.3 Space derivatives with non-uniform filter width

Alternatively, we can re-derive Eq. (A-8) assuming the filter function is dependent on the local position, *i.e.*, $\Delta_f(\vec{x})$, following the work of Ghosal and Moin [101] for spatial filtering on non-uniform meshes for use with LES. This may be convenient in practice since for structured grids the filter width is often associated with a multiple size of the local grid size. In order to derive an analogous expression as in Eq. (A-8) for non-uniform grids, we can define a filter in computational space, $G^*[(\eta_k - \eta'_k)/\Delta_{f_T}]$ that is characterized by a fixed filter width, Δ_{f_T} in the transformed space where the transformed coordinate variable, $\vec{\eta}$, is related to the physical coordinate, $\vec{x}$, through the relation $\vec{\eta} = \vec{F}(\vec{x})$. A complementary transformation from computational space to physical space is defined by the function, $\vec{f}$, defined as: $\vec{x} = \vec{f}(\vec{\eta})$. Figure A-2 illustrates the use of these transformations assuming a top-hat function for g of width, $\Delta_{f_T} = 5\Delta\eta$, where $\Delta\eta$ is the discretization of the mesh.

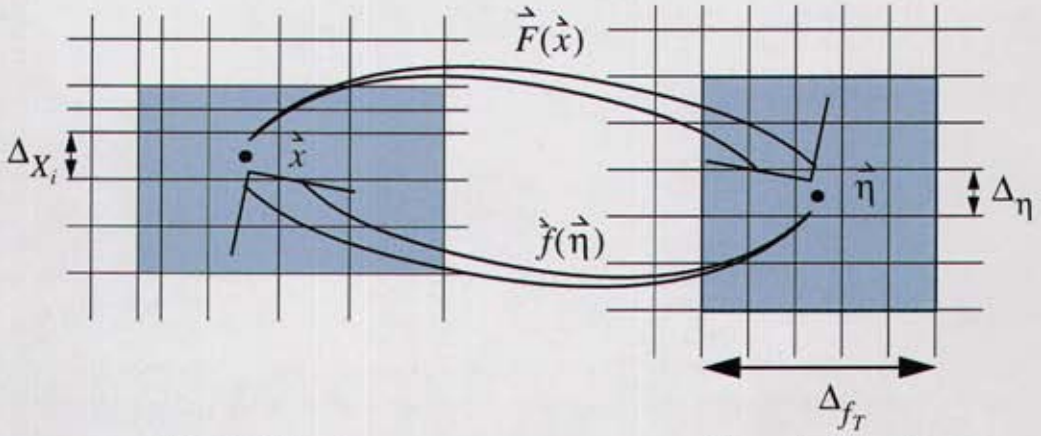

Figure A -2 Relationship between phase-averaging on computational space and physical space on non-uniform grids.

The derivation of an expression that is equivalent to Eq. (A-8) for non-uniform filtering begins with the definition of the gradient of a phase averaged vector quantity in transformed space using the new definition of the filtering function,

$$\frac{\partial}{\partial x_j}\langle\beta_j(x_i)\rangle = \frac{\partial}{\partial x_j}\int_{V_{g_{T_\infty}}} \beta_j(\eta'_k)G^*\left(\frac{\eta_k-\eta'_k}{\Delta_{f_T}}\right)dV'_T$$
$$= \frac{\partial}{\partial x_j}\int_{V_{g_\infty}} \beta_j[F_k(x'_p)]G^*\left(\frac{F_k(x_i)-F_k(x'_p)}{\Delta_{f_T}}\right)J(x'_p)dV' \qquad \text{(A-9)}$$

where the quantity, J, is the Jacobian defined as: $J = |\partial F_p/\partial x_q|$ and defines the ratio of the computational $(dV_T)$to physical (dV) differential volumes. Carrying the differential operation inside the integral of Eq. (A-9) leads to,

$$\frac{\partial}{\partial x_j}\langle\beta_j(x_i)\rangle = \int_{V_{g_\infty}} \beta_j[F_k(x'_p)]\frac{\partial}{\partial x_j}\left[G^*\left(\frac{F_k(x_i)-F_k(x'_p)}{\Delta_{f_T}}\right)\right]J(x'_p)dV' \qquad \text{(A-10)}$$

and observing that the partial derivative of G with respect to x_j defined as, $\frac{\partial G^*}{\partial x_j} = \frac{\partial G^*}{\partial(\ldots)}\frac{\partial(\ldots)}{\partial x_j} = \frac{\partial G^*}{\partial(\ldots)}\frac{\partial F_k}{\partial x_j}$, is similar to the partial derivative of G^* with respect to x'_p, $\frac{\partial G^*}{\partial x'_p} = \frac{\partial G^*}{\partial(\ldots)}\frac{\partial(\ldots)}{\partial x'_p} = -\frac{\partial G^*}{\partial(\ldots)}\frac{\partial F_k}{\partial x'_p}$, with the only difference being the change in signs and the grid metrics. Using this information, the following relation can be obtained.

$$\frac{\partial G^*}{\partial x_j} = \frac{\partial G}{\partial x'_p}\frac{\partial F_k}{\partial x_j}\left(\frac{\partial F_k}{\partial x_p}\right)^{-1} = \frac{\partial G^*}{\partial x'_p}\frac{\partial F_k}{\partial x_j}\frac{\partial f_p}{\partial \eta_k} \qquad \text{(A-11)}$$

Substituting Eq. (A-11) into Eq. (A-10) and dropping the dependency arguments leads to:

$$\frac{\partial}{\partial x_j}\langle\beta_j\rangle = -\int_{V_{g_\infty}} \beta_j\frac{\partial G^*}{\partial x'_p}\frac{\partial F_k}{\partial x_j}\frac{\partial f_p}{\partial \eta_k}JdV'. \qquad \text{(A-12)}$$

Integrating Eq. (A-12) by parts (*i.e.*, $\beta_j\partial G^*/\partial x'_p = \partial(\beta_j G^*)/\partial x'_p - G^*\partial\beta_j/\partial x'_p$) then the following expression is obtained.

$$\frac{\partial}{\partial x_j}\langle\beta_j\rangle = \int_{V_{g_\infty}} \frac{\partial\beta_j}{\partial x'_p}G\frac{\partial F_k}{\partial x_j}\frac{\partial f_p}{\partial \eta_k}JdV' - \int_{V_{g_\infty}} \frac{\partial}{\partial x'_p}[\beta_j G^*]\frac{\partial F_k}{\partial x_j}\frac{\partial f_p}{\partial \eta_k}JdV'$$
$$= \frac{\partial F_k}{\partial x_j}\int_{V_{g_\infty}} \frac{\partial\beta_j}{\partial x'_p}\frac{\partial f_p}{\partial \eta_k}G^*JdV' - \frac{\partial F_k}{\partial x_j}\int_{V_{g_\infty}} \frac{\partial}{\partial \eta_k}[\beta_j G^*]dV_T' \qquad \text{(A-13)}$$

Recognizing the first term in Eq. (A-13) is *not* equal to the phase average derivative of β_j, *i.e.*, $\langle\partial\beta_j/\partial x_j\rangle = \int_{V_{g_\infty}} (\partial\beta_j/\partial x'_j)G^*JdV$. The difference between these terms is defined as the

commutation error, CE, and can be shown of $O(\Delta_{f_T}^2)$ in magnitude (see Appendix B for proof). One can minimize this error by choosing the filtering function, G^*, to satisfy certain moment conditions to diminish the CE to arbitrarily small levels [103, 104]. However, for this application this error can be ignored since the CE will most likely be less than the truncation error associated with the convective schemes. Employing the divergence theorem to the second term in Eq. (A-13) then the volume integral can be expressed in terms of a surface integral along the liquid droplet surface, A_l, for which we arrive at a surface integral that is analogous to the surface integral term in Eq. (A-8) so that Eq. (A-13) is expressed as:

$$\frac{\partial}{\partial x_j}\langle \beta_j \rangle = \langle \frac{\partial \beta_j}{\partial x_j} \rangle + \underbrace{\int_{V_{g_\infty}} G^* \frac{\partial \beta_j}{\partial x'_p}\left[\delta_{jp} - \frac{\partial F_k}{\partial x_j}\frac{\partial f_p}{\partial \eta_k}\right] JdV'}_{\text{CE}} - \frac{\partial F_k}{\partial x_j}\int_{A_l} \beta_j G^* dA'_{T_j} \qquad \text{(A-14)}$$

where the CE is explicitly noted. Also, note the area integral in Eq. (A-14) is not intuitive as the previous surface integral of Eq. (A-8). This term involves integration around the surface of the droplets in transformed space multiplied by a grid metric evaluated at the filtering point of interest, x_i, and developing constitutive models for the effects of SGS spray would be exceptionally challenging. Adding and subtracting a surface integral involving integration in physical space then Eq. (A-14) can be re-written as:

$$\frac{\partial}{\partial x_j}\langle \beta_j \rangle = \langle \frac{\partial \beta_j}{\partial x_j} \rangle + \underbrace{\int_{V_{g_\infty}} G^* \frac{\partial \beta_j}{\partial x'_p}\left[\delta_{jp} - \frac{\partial F_k}{\partial x_j}\frac{\partial f_p}{\partial \eta_k}\right] JdV'}_{\text{CE}} \qquad \text{(A-15)}$$

$$\underbrace{-\frac{\partial F_k}{\partial x_j}\int_{A_l} \beta_j G^* dA'_j}_{\text{SET}} + \underbrace{\frac{\partial F_k}{\partial x_j}\left\{\int_{A_l} \beta_j G^* dA'_j - \int_{A_l} \beta_j G^* dA'_{T_j}\right\}}_{\text{SEET}}$$

for which the last two terms represent the surface exchange term (SET) that is independent of the transformation grid metrics and a surface exchange error term (SEET). The SET term is basically the same surface exchange term of Eq. (A-8) for uniform grids for which well known constitutive models exist. The SEET accounts for the error in approximating the surface integral in physical space. Further analysis could identify the leading order SEET error term using a Taylor series expansion, analogous to the CE. However, any error would be unacceptable since conservation of mass, momentum and energy would be violated between the phases.

In summary, the use of non-uniform filters is desirable from a CFD implementation standpoint. However, the introduction of non-uniform filters introduces two difficult to treat

issues. The first is commutation error and the second is the surface integral term that is expressed in terms of transformed computational space for which constitutive properties are not easily obtained. The second of these terms can be simply expressed in terms of surface integrals in physical space, however then a SEET is introduced for which conservation principals would potentially be violated. For these reasons, a uniform filtering approach is pursued to develop the phase-averaged transport equations.

A.2 Phase Averaged Conservation Equations

Applying the phase-averaging relations summarized in Eqs. (A-4) and (A-8) to the governing transport equations of mass, momentum and energy results in the phase averaged transport equations.

A.2.1 Conservation of Mass

$$\frac{\partial(\phi\hat{\rho})}{\partial t} + \frac{\partial(\phi\hat{\rho}\tilde{u}_k)}{\partial x_k} = \underbrace{\int_{A_d} \rho(u_k - v_k) G n_k dA_d}_{\textit{mass transfer at the droplet surface}} \tag{A-16}$$

A.2.2 Conservation of Species

$$\frac{\partial(\phi\hat{\rho}\tilde{Y}_i)}{\partial t} + \frac{\partial(\phi\hat{\rho}\tilde{u}_k\tilde{Y}_i)}{\partial x_k} = \frac{\partial(\phi q_{m_k}(\hat{D}_m, \tilde{T}))}{\partial x_k} + \underbrace{\langle \dot{\omega}_i''' \rangle}_{\textit{phase-averaged gas-phase reaction rate}}$$

$$+ \underbrace{\frac{\partial[\langle \rho u_k \tilde{Y}_i \rangle - \phi\hat{\rho}\tilde{u}_k\tilde{Y}_i]}{\partial x_k}}_{\textit{subgrid macroscopic species dispersion}} + \underbrace{\frac{\partial}{\partial x_k}[\phi(\hat{q}_{m_k} - q_{m_k}(\hat{D}_m, \tilde{T}))]}_{\textit{subgrid microscopic species dispersion}} \tag{A-17}$$

$$+ \underbrace{\int_{A_d} [\rho(u_k - v_k) Y_{ik} + q_{m_k}] G n_k dA_d}_{\textit{species mass transfer at the droplet surfaces}}$$

A.2.3 Conservation of Momentum

$$\frac{\partial(\phi\hat{\rho}\tilde{u}_j)}{\partial t}+\frac{\partial(\phi\hat{\rho}\tilde{u}_j\tilde{u}_i)}{\partial x_i}=-\frac{\partial(\phi\hat{p})}{\partial x_j}+\frac{\partial(\phi\tau_{ij}(\tilde{u}_i,\tilde{u}_j,\hat{\mu}))}{\partial x_i}+g\phi(\rho_\infty-\hat{\rho})$$
$$+\underbrace{\frac{\partial[\langle\rho u_j u_k\rangle-\phi\hat{\rho}\tilde{u}_j\tilde{u}_k]}{\partial x_k}}_{\textit{subgrid macroscopic momentum dispersion}}+\underbrace{\frac{\partial(\langle\tau_{ij}\rangle-\phi\tau_{ij}(\tilde{u}_i,\tilde{u}_j,\hat{\mu}))}{\partial x_i}}_{\textit{subgrid microscopic momentum dispersion}} \qquad \text{(A-18)}$$
$$+\underbrace{\int_{A_l}[\rho u_j(u_i-v_i)+p\delta_{ij}-\tau_{ij}]Gn_i dA}_{\textit{momentum transfer at the droplet surfaces}}$$

A.2.4 Conservation of Energy (low Mach number formulation)

$$\frac{\partial(\phi\hat{\rho}\hat{h})}{\partial t}+\frac{\partial(\phi\hat{\rho}\hat{h}\tilde{u}_i)}{\partial x_i}=-\frac{\partial(\phi q_k(\hat{k},\hat{T}))}{\partial x_k}$$
$$+\underbrace{\frac{\partial[\langle\rho h u_k\rangle-\phi\hat{\rho}\hat{h}\tilde{u}_k]}{\partial x_k}}_{\textit{subgrid macroscopic thermal dispersion}}+\underbrace{\langle\tau_{ij}\frac{\partial u_i}{\partial x_j}\rangle}_{\textit{phase-averaged viscous dissipation rate}} \qquad \text{(A-19)}$$
$$+\underbrace{\int_{A_l}[\rho h(u_i-v_i)-\tau_{ij}(\partial u_i/\partial x_j)+q_k]Gn_i dA}_{\textit{heat and work transfer at the droplet surface}}$$
$$\underbrace{\langle\dot{Q}_{rad}\rangle+\langle\dot{Q}_{com}\rangle}_{\textit{phase-averaged gas-phase radiation and combustion}}$$

As shown in Eqs. (A-16) - (A-19), the use of phase averaging introduces unknown subgrid correlations and surface integral terms that will require explicit closure models. The details of these closures for all of these various terms are not discussed in detail in this report. Many of the closures for the phase averaged non-linear source terms and second order dispersion correlation terms are either ignored or expressed in terms of phase-averaged quantities, which are appropriate for the relatively dispersed sprays used in fire simulations. The purpose of deriving Eqs (A-16)- (A-19) is to identify the surface integral terms responsible for the first order effects of mass, momentum and energy exchange between the gas and liquid phases of

the system. The velocity difference, $u_k - v_k = w_k$, in those equations represents the velocity of the mass, momentum and energy through the droplet surface with respect to a coordinate system fixed to the droplet surface. The integrated value of this quantity around a the surface of the droplet, A_d, multiplied times an intrinsic property then represents a net gain or loss of that property for the droplet. These surface integrals can be related to the mass, momentum and energy droplet source terms of chapter 2 as follows:

$$\int_{A_l} \rho(u_k - v_k) G n_k dA = -\sum_{n_d} G\dot{m}$$

$$\int_{A_l} [\rho u_j(u_i - v_i) + p\delta_{ij} - \tau_{ij}] G n_i dA = -\sum_{n_d} G[u_{d_j}\dot{m}_d + m_d F_{D_j}] \qquad \text{(A-20)}$$

$$\int_{A_l} [\rho h(u_i - v_i) - \tau_{ij}(\partial u_i/\partial x_j)] G n_i dA = -\sum_{n_d} G[\dot{Q}_c + \dot{m}_d h_g]$$

where the filter function, G, is evaluated at the of the drop since it is assumed that G doesn't vary very much over the surface of an individual droplet. In addition, if G is taken at the volume of the computational cell, then we recover the source terms that are shown in Table 2-1.

It should also be noted that only principles of phase-averaging have been reviewed in this report. Implementation into VULCAN requires that the phase-averaged equations also be time averaged to be consistent with the RANS formulation. Deriving a closed form of phase and time averaged set of equations for two-phase flows is still an active area of research and the details are outside the scope of this report. Interested readers can find some of these details in Refs. [107-111].

APPENDIX B COMMUTATION ERROR ORDER OF ACCURACY

The following summarizes the derivation for determining the leading order terms for the commutation error, *CE*, introduced in Appendix A, defined as:

$$CE = \int_{V_{g_\infty}} G^*\left(\frac{F_k(x_i) - F_k(x'_p)}{\Delta_{f_T}}\right)\frac{\partial \beta_j}{\partial x'_p}(x'_p)\left[\delta_{jp} - \frac{\partial F_k}{\partial x_j}(x_i)\frac{\partial f_p}{\partial \eta_k}(F_k(x'_p))\right]J(x'_p)dV' \tag{B-1}$$

$$= \int_{V_{g_\infty}} G^*\left(\frac{\eta_k - \eta'_k}{\Delta_{f_T}}\right)\frac{\partial \beta_j}{\partial x'_p}(f_p(\eta'_k))\left[\delta_{jp} - \frac{\partial F_k}{\partial x_j}(f(\eta_k))\frac{\partial f_p}{\partial \eta_k}(\eta'_k)\right]dV_T'$$

To find an estimate of the *CE*, the $\partial\beta_j/\partial x'_p$ and $\partial f_p/\partial \eta_k$ terms are expanded about the point η_k using the following definitions of Taylor series expansions in multidimensions [102].

$$\frac{\partial f_p}{\partial \eta'_k}(\eta'_k) = \sum_{n=0}^{\infty}\frac{1}{n!}\left(\Delta\eta'_r\frac{\partial}{\partial \eta_r}\right)^n\frac{\partial f_p}{\partial \eta_k}(\eta_k)$$

$$\frac{\partial \beta_j}{\partial x'_p}(f_p(\eta'_k)) = \sum_{m=0}^{\infty}\frac{1}{m!}\left(\Delta\eta'_s\frac{\partial}{\partial \eta_s}\right)^m\frac{\partial \beta_j}{\partial x_p}(f_p(\eta_k)) \tag{B-2}$$

where $\Delta\eta'_i$ $(= \eta'_i - \eta_i)$ is the difference between the filtering point of interest and a location within the filtering volume as illustrated in Fig. B-1. The differential terms in the summations of Eq. (B-2) are shorthand notations for a differential operator in three dimensions for a Cartesian coordinate system.

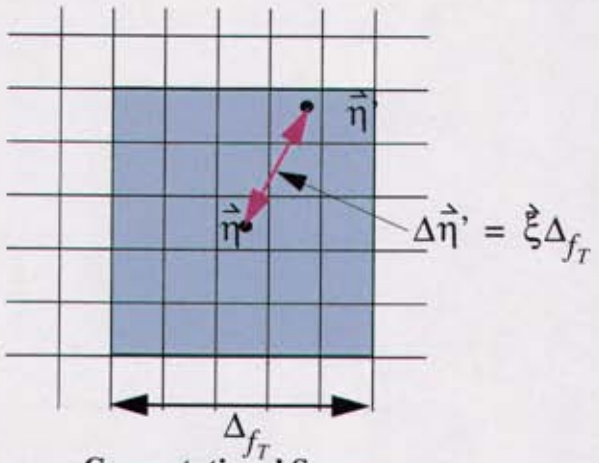

Figure B -1 Taylor series expansion of functions in Eq.(B-1) around the filtering point of interest.

Substituting the expansions of Eq. (B-2) into Eq. (B-1) and redefining the expansion parame-

ter as $\Delta\eta' = \xi\Delta_{f_T}$ where $0 < \xi < 1$, then the commutation error can be expressed in terms of two components with leading order terms explicitly expressed in terms of the filter width [101].

$$CE = \int_{V_{g_\infty}} G\left(\sum_{m=0}^{\infty} \frac{1}{m!}\left(\Delta_{f_T}\xi_s \frac{\partial}{\partial\eta_s}\right)^m \frac{\partial\beta_j}{\partial x_p}\right)\delta_{jp}dV_T' \\ \frac{\partial F_k}{\partial x_j}\int_{V_{g_\infty}} G^*\left[\sum_{m=0}^{\infty}\sum_{n=0}^{\infty}\frac{1}{n!}\frac{1}{m!}\Delta_{f_T}^{m+n}\left(\xi_r\frac{\partial}{\partial\eta_r}\right)^n\frac{\partial f_p}{\partial\eta_k}\left(\xi_s\frac{\partial}{\partial\eta_s}\right)^m\frac{\partial\beta_j}{\partial x_p}\right]dV_T' \tag{B-3}$$

Recognizing that for $n = 0$, the second term in Eq. (B-3) term cancels the first term allows for the commutation error to be expressed as a single double summation.

$$CE = \frac{\partial F_k}{\partial x_j}\int_{V_{g_\infty}} G^*\left[\sum_{m=0}^{\infty}\sum_{n=1}^{\infty}\frac{1}{n!}\frac{1}{m!}\Delta_{f_T}^{m+n}\left(\xi_r\frac{\partial}{\partial\eta_r}\right)^n\frac{\partial f_p}{\partial\eta_k}\left(\xi_s\frac{\partial}{\partial\eta_s}\right)^m\frac{\partial\beta_j}{\partial x_p}\right]dV_T' \tag{B-4}$$

In addition, since G is an even function, then the first non-zero term of Eq. (B-4) is for $m = n = 1$ resulting in a leading truncation error of $O(\Delta_{f_T}^2)$ consistent with the findings of Ghosal *et al.* [101].

DISTRIBUTION

1 National Institute of Standards and Technology
Attn: D. Gann
Fire Science Division
Building and Fire Research Laboratory
100 Bureau Drive, Stop 8650
Gaithersburg, MD 20899-8650

2 Office of the Secretary of Defense, DOT/LFT&E
Attn: T. Christie, R. Wojciechowski, R. Seymour
Room 1C730
1700 Defense Pentagon
Washington, DC 20301-1700

1 Aerospace Survivability Flight
Attn: M. Lentz
46OG/OGM/OL-AC
Bldg. 1661B, Area B
Wright Patterson Air Force Base, OH 45433-7605

1 Air Force Aeronautical Systems Center
Attn: Hugh Griffis
Bldg. 11a, Room 101H
1970 Monahan Way
Wright Patterson Air Force Base, OH 45433-7208

1 USDOE-HQ, Defense Programs
Attn: B. Froh
DP-45,GTN
19901 Germantown Road
Germantown, MD 20874-1290

1 JTCG/AS Central Office
Attn: J. Jolley
Director, Vulnerability Reduction Subgroup
Crystal Square Four, Suite 1103
1213 Jefferson Davis Hwy.
Arlington, VA 22202-4304

1 NAWCWPNS
Attn: L. Budd
Code 418300D
1 Administration Circle
China Lake, CA 93555-6100

1 INS Inc
Attn: D. Keyser
48015-A Pinehill Run Rd.
Lexington Park, MD 20653

1 Federal Aviation Administration
Attn: G. Sarkos
Manager, Fire Safety Section
William J. Hughes Technical Center
AAR-422
Atlantic City International Airport, NJ 08405

1 Army Research Laboratory
Attn: R. Skaggs
AMSRL-WM-TB
Aberdeen Proving Ground, MD 21001

1 Army Research Laboratory
Attn. A. Miziolek
AMSRL-WM-BD
Aberdeen Proving Ground, MD 21001

1 Naval Research Laboratory
Attn. R. Sheinson
Code 6185
4555 Overlook Ave., S.W.
Washington, DC, 20375-5342

1	MS 1135	J. T. Nakos, 9132
1	MS0748	S. P. Nowlen, 6413
5	MS 0821	L. A. Gritzo, 9132
1	MS 0824	J. L. Moya, 9130
1	MS 0824	A. C. Ratzel, 9110
1	MS 0834	D. J. Rader, 9112
1	MS 0828	M. Pilch, 9133
1	MS 0828	A. R. Black, 9133
1	MS 0834	T. Y. Chu, 9100
1	MS 0835	S. N. Kempka, 9141
1	MS 0835	R. J. Cochran, 9141
1	MS 0835	S. P. Domino, 9141
1	MS 0836	M. R. Baer, 9100
1	MS 0836	E. S. Hertel, 9116
1	MS 0836	M. L. Hobbs, 9116
10	MS 1135	P. E. DesJardin, 9132
1	MS 0836	V. G. Figueroa, 9132
1	MS 0836	W. Gill, 9132
1	MS 0836	V. F. Nicolette, 9132
1	MS 1135	J. M Suo-Anttila, 9132
1	MS 0836	S. R. Tieszen, 9132
1	MS 0836	J. M. Nelsen, 9132
1	MS 0836	K. A. Jensen, 9132
1	MS 0841	T. C. Bickel, 9100
1	MS 9042	C. D. Moen, 8728
1	MS 9042	G. H. Evans, 8728
1	MS 9051	A. R. Kerstein, 8351
1	MS 9051	J. C. Oefelein, 8351

1	MS 9018	Central Technical Files, 8945-1
2	MS 0899	Technical Library, 9616
1	MS 0612	Review and Approval desk, 9612, For DOE/OSTI